Eur. Phys. J. A **35**, 221–242 (2008)
DOI 10.1140/epja/i2007-10546-7

THE EUROPEAN PHYSICAL JOURNAL A

Regular Article – Theoretical Physics

Hadron production and phase changes in relativistic heavy-ion collisions

J. Letessier[1,2] and J. Rafelski[1,2,3,a]

[1] Department of Physics, University of Arizona, Tucson, AZ, 85721 USA
[2] Laboratoire de Physique Théorique et Hautes Energies, Université Paris 7, 2 place Jussieu, F-75251 Cedex 05, Paris, France
[3] CERN-PH-TH, 1211 Geneva 23, Switzerland

Received: 25 October 2007 / Revised: 7 February 2008
Published online: 11 March 2008 –
Communicated by T. Bíró

Abstract. We study soft hadron production in relativistic heavy-ion collisions in a wide range of reaction energy, $4.8\,\mathrm{GeV} < \sqrt{s_{\mathrm{NN}}} < 200\,\mathrm{GeV}$, and make predictions about yields of particles using the statistical hadronization model. In fits to experimental data, we obtain both the statistical parameters as well as physical properties of the hadron source. We identify the properties of the fireball at the critical energy threshold, $6.26\,\mathrm{GeV} < \sqrt{s^{\mathrm{cr}}_{\mathrm{NN}}} < 7.61\,\mathrm{GeV}$, marking for higher energies the hadronization of an entropy-rich phase. In terms of the chemical composition, one sees a phase which at low energy is chemically under-saturated, and which turns into a chemically over-saturated state persisting up to the maximum accessible energy. Assuming that there is no change in physical mechanisms in the energy range $15 > \sqrt{s_{\mathrm{NN}}} \geq 200\,\mathrm{GeV}$, we use continuity of particle yields and statistical parameters to predict the hadron production at $\sqrt{s_{\mathrm{NN}}} = 62.4\,\mathrm{GeV}$, and obtain total yields of hadrons at $\sqrt{s_{\mathrm{NN}}} = 130\,\mathrm{GeV}$. We consider, in depth, the pattern we uncover within the hadronization condition, and discuss possible mechanisms associated with the identified rapid change in system properties at $\sqrt{s^{\mathrm{cr}}_{\mathrm{NN}}}$. We propose that the chemically over-saturated $2+1$ flavor hadron matter system undergoes a 1st-order phase transition.

PACS. 24.10.Pa Thermal and statistical models – 25.75.-q Relativistic heavy-ion collisions – 13.60.Rj Baryon production – 12.38.Mh Quark-gluon plasma

1 Introduction

It is believed that the deconfined phase of matter is formed at sufficiently high energy and reaction volume reached in the most central collisions of heavy ions at the top RHIC energy [1]. The question is where this critical energy threshold $\sqrt{s^{\mathrm{cr}}_{\mathrm{NN}}}$ is. We pursue this point in this systematic study, in order to explore possible phase changes occurring as a function of collision energy [2]. We furthermore compare our results qualitatively to the behavior seen as a function of the reaction volume [3].

The tool, used in our study of soft hadron production, is the generalized statistical hadronization model (SHM) which allows for particle yields to be in full chemical non-equilibrium [4]. SHM is capable to describe, in detail, hadron abundances and has been considerably refined in past decade, after its formulation by Fermi and Hagedorn [5].

We present and/or extend here the results of the analysis of the energy dependence of total hadron production yields for:

a) fixed target symmetric Au–Au reactions at the top available AGS projectile energy 11.6 AGeV (energy per colliding nucleon pair $\sqrt{s_{\mathrm{NN}}} = 4.84\,\mathrm{GeV}$),
b) fixed target symmetric Pb–Pb reactions at SPS at 20, 30, 40, 80 and 158 AGeV projectile energy. This we refer to as SPS energy range, $6.26 \leq \sqrt{s_{\mathrm{NN}}} \leq 17.27\,\mathrm{GeV}$,
c) the Au–Au reactions in the collider mode at RHIC in $65+65$, $100+100$, and also at $31.2+31.2$ AGeV reactions for both total, and central rapidity yields. This is the RHIC energy range, $62.4 \leq \sqrt{s_{\mathrm{NN}}} \leq 200\,\mathrm{GeV}$.

Experimental data analysis at RHIC was carried out for the central rapidity region yields at $\sqrt{s_{\mathrm{NN}}} = 130$ and 200 GeV, and for the full hadron yields at 200 GeV. The results we present for the total hadron yields at $\sqrt{s_{\mathrm{NN}}} = 130\,\mathrm{GeV}$ and $62.4\,\mathrm{GeV}$, arise from our model considerations alone. This is also in part the case for the central rapidity yields at $\sqrt{s_{\mathrm{NN}}} = 62.4\,\mathrm{GeV}$.

As a first step, we aim to describe at each reaction energy the hadron yield data. We obtain in this process the statistical hadronization model (SHM) parameters, which allow to evaluate the yields of all (also of unobserved) particles. One can see SHM analysis as a method of how

[a] e-mail: rafelski@physics.arizona.edu

the known experimental hadron yield data can be extrapolated to obtain the unobserved hadron yields. For this reason, we also attempt to extrapolate to reaction energies and phase space coverage which, for lack of data, is not allowing a SHM fit. For example, for the $31.2+31.2\,A$GeV case, we interpolate strange particle yields, which are known below and above this energy, and/or fix certain SHM parameters which show continuity as a function of reaction energy, respecting in the process the constraints of the SHM.

In our analysis, we are seeking consistency in the results across the reaction energy. This is of importance when the number of measurements is not much greater than is the number of observables. When we are able to fix the values of statistical parameters by consistency check across the energy range, then the number of used parameters is reduced and the statistical significance shown in this work is for the number of parameters actually fitted. However, more often, in the study of statistical significance, we do not account explicitly for consistency across the energy range. For this reason, in most cases, the statistical significance we present is a lower limit.

Once a statistically significant description of the data sample at an energy is achieved, we have available the yields of all soft hadronic particles and their resonances. We sum partial contributions of each particle species to quantities such as entropy, strangeness, baryon number, to obtain the properties of the fireball at the time of particle production (hadronization). In this way, we evaluate fireball breakup pressure, entropy, baryon number, strangeness yield and the thermal energy content. In this approach, the kinetic energy content associated with the collective flow of matter is not considered —this requires a study of particle $m_\perp$ and rapidity spectra, beyond the integrated hadron yields.

High strangeness [6], and entropy content [7,8] of a dense hadronic matter fireball are the anticipated characteristic property of the color deconfined state of matter. Once formed, this enhancement of strangeness and entropy is also the property of the final hadronic state: first principles require that entropy must increase in the fireball expansion, as well as in the ensuing hadronization process; model studies show that once strangeness is produced, it remains present during expansion of dense matter, it can slightly increase during hadronization [9,10].

Particle yields, and pion yield, in particular, provide a natural measure of the entropy yield, while the kaon yields, and in particular the K^+ yield, are an approximate measure of the total strangeness yield across all reaction energies [7]. The yield ratio K^+/π^+ has been studied as a function of the reaction energy in the SPS energy domain and a strong "horn" like feature has been discovered [2].

This suggests a change in the reaction mechanism of particle production, occurring in central collisions of Pb–Pb, in the energy interval $6.26\,\mathrm{GeV} \leq \sqrt{s_{\mathrm{NN}}} \leq 7.61\,\mathrm{GeV}$, the two limits correspond to 20 and, respectively, 30 AGeV Pb beams on a fixed target. This energy range is just at the predicted threshold of quark-gluon formation arising considering the balance of energy deposition and relativistic reaction dynamics [11]. The possibility of a rich phase structure of the deconfined phase at high baryochemical potential and finite temperature further furthers the interest in the study of this reaction energy domain [12].

To describe experimental results indicating the presence of a critical ("cr") energy threshold, one can, in first instance, use two different reaction models which apply below and, respectively, above a postulated energy threshold for a phase transformation [13]. However, this presupposes the most important outcome, namely that there is an energy-dependent change in the dense matter fireball structure at its breakup. Moreover, such an approach does not produce as result of the analysis an insight into the structural change that occurs, and which could be compared with predictions. Instead, the structural change is part of the hypothesis under which the analysis is carried out. For this reason, the methodology we choose here is more general.

We use in this work the software package SHARE (statistical hadronization with resonances) [14], the public SHM suit of programs, where the methods of SHM analysis are described in greater detail. Of particular importance here is that the full mass spectrum of hadron resonances is included [15]. SHARE implements two features important for the full understanding of the K^+/π^+ horn:

1) the isospin asymmetry driven by proton–neutron asymmetry, which is particularly relevant at low reaction energies,
2) the chemical non-equilibrium (phase space undersaturation and over-saturation) for strange and light quarks.

These two features appear to be essential to obtain a description of the K^+/π^+ energy-dependent yield.

We first describe, in the next sect. 2, features of the data sample we use, discuss the input data and results of the fits for the AGS/SPS and RHIC energy range separately. We discuss the resulting statistical parameters and the confidence level of our fits. We survey, in both tabular and graphic form, the energy dependence of the particle yields of interest, including an explanation of the K^+/π^+ horn. We then discuss the physical properties of the fireball at the point of chemical freeze-out in sect. 3, show the energy dependence of the model parameters and of the physical properties, and address the strangeness and entropy production. We discuss the results of our analysis and present their interpretation in the final sect. 4.

2 Fit procedure and hadron multiplicities

2.1 General remarks

The measured experimental results are available for either total particle yields, $N_{4\pi}$, or for central rapidity yields, $\mathrm{d}N/\mathrm{d}y$. At RHIC energy scale, we will study both data sets, though $N_{4\pi}$ is rather incomplete at this time. At AGS and SPS, we will solely consider $N_{4\pi}$, in order to

minimize the impact of the shape of the longitudinal unstopped matter flow on the outcome of the analysis.

At SPS, a semi-distinct central rapidity domain is only present in the top SPS case, its consideration will make good sense once the RHIC $\mathrm{d}N/\mathrm{d}y$ data extend to the minimum accessible energy domain which is close to top SPS energy range. However, this will require the introduction of models of collective matter flow, a step which we do not wish to take in this work. At high RHIC energies, we presume that the fragmentation regions are sufficiently separated from the central rapidity domain as to allow the study of the rapidity particle distributions $\mathrm{d}N/\mathrm{d}y$, at central rapidity, in a model-independent fashion.

We include, in our consideration of the total particle yields $N_{4\pi}$, the trigger condition which defines the participant "wounded" nucleon number N_{W}. This has to be equal to the total net baryon number $b = B - \overline{B}$ contained within the final-state particle multiplicities. Furthermore, both for $N_{4\pi}$ and central rapidity yields $\mathrm{d}N/\mathrm{d}y$, we consider two constraints:

a) the fraction of protons among all nucleons (0.39 for heavy nuclei) establishes a fixed final ratio of all electrical charge Q to the total final-state baryon number b —the ratio Q/b is preserved in any fraction of a volume of centrally colliding nuclei; it is a measured quantity given the fact that both target and projectile are known;
b) strangeness (valence s-quarks) content of hadrons prior to weak decays has to be (up to systematic experimental error) balanced by antistrangeness (valence $\bar{s}$-quarks) bound in hadrons for the $N_{4\pi}$ study, and nearly balanced when considering the central rapidity $\mathrm{d}N/\mathrm{d}y$ distributions.

As our prior studies showed [16], any deviation from strangeness conservation as a function of rapidity is, in general, smaller than the typical 10% systematic error of the experimental data points. It is the level of systematic error in the particle yields which determines the precision at which we have to assure strangeness conservation. Forcing exact balance can create an aberration of the fit, since the sharp constraint is inconsistent with several independent measurements which contribute to the cancellation. For example, at several SPS energies the systematic errors between K^+ and Λ which control the yields of $\bar{s}$ and, respectively, s quarks, do not cancel to better than 8% level. This can be checked without a fit in a qualitative study of the key particle yields.

Another reason to be cautious with the strangeness conservation is that the spectra of hadrons we are using could contain wrong entries (*e.g.*, pentaquark states which we in view of recent experimental results do not anymore include in the input data set, or wrong spin-isospin assignments for little known states), or some relevant undiscovered resonances maybe missing in the hadron spectrum. These effects are largest when the baryon asymmetry is most visible, since the strangeness balance condition probes at large baryochemical potential the mass spectrum of strange baryons and mesons separately, with mesons dominating in antistrangeness and baryons important in the strangeness count.

For this reason, our strangeness conservation procedure is as follows: when a first fit shows a slight strangeness asymmetry, we find the best parameters for the fit with a loose, systematic-error–related strangeness conservation constraint allowing, *e.g.*, a 10% deviation from balance as a fit input, that is we request $(s-\bar{s})/(s+\bar{s}) = 0 \pm 0.1$. Since we present confidence level and profiles of the fit, and we wish to have from energy to energy comparable results, we redo the fit with a fixed preferred value of the strangeness fugacity λ_s as is done in case of using exact strangeness conservation.

In this way, we obtain a data fit within the same approach as for the cases where exact strangeness conservation is used to fix one parameter, so that confidence levels are comparable. We find $-0.07 > (s-\bar{s})/(s+\bar{s}) > -0.1$ in the SPS energy domain. The asymmetry favors an overcount of $\bar{s}$-quarks in emitted hadrons. It is moderate in its relative magnitude, staying within the systematic errors of the measurements used in this study. We will state the strangeness balance explicitly when presenting the computed particle yields. Note that addition of pentaquarks to the hadron spectrum decreases this asymmetry by 0–3%, but has otherwise minimal influence on the fit results presented.

As the above discussion of strangeness conservation shows, conserved quark quantum numbers introduce yield constraints, which particle multiplicities cannot deviate from. We further recall that a subset of SHM parameters determine a set of particle ratios, as has been shown for the first time in 1982 [17]. A nice example is the chemical relation between the K^-/K^+ and $\bar{p}/p$ demonstrated experimentally in 2003, see fig. 4 in [18], a development based on the rediscovery of the SHM constraints in 2000 [19]. Since SHM with its chemical consistencies has been very successful in helping understand hadron production, we embark on further data verifications at each energy, checking the consistency of experimental data with SHM.

A suspect particle yield can be further cross-checked studying the behavior of this particle yield as a function of energy. Such consideration is very important since we are searching for a change in the physical properties of the fireball as a function of energy, and we do not want the outcome to be even in part the result of a statistical fluctuation in the reported yield of a subset of particles. We find inconsistencies (see next paragraph) in the particle yield effects. None of these influence decisively the findings we report here, in part because of the more lax attitude we take toward the constraint on strangeness conservation we described above. Moreover, considering the large number of experimental data considered, fluctuations in experimental data sample must occur.

As result of this analysis, we did not use the $\Lambda(1520)$ nor Ω and $\overline{\Omega}$ yields obtained at 158 AGeV in our fit. The preliminary $\Lambda(1520)$ value at top SPS is $\Lambda(1520) = 1.45 \pm 0.4$ [20]. This is within 3 s.d. of the SHM yield. However, this exceptionally narrow resonance may be subject to additional effects [21] and we felt that it is more pru-

Table 1. The input $N_{4\pi}$ total particle multiplicities data at top, and, below, the resulting statistical parameters for AGS and SPS energy range. At the bottom, we state the chemical potential corresponding to the central values of the fugacities. For each projectile energy E [AGeV], we also present in the header the invariant center-of-momentum energy per nucleon pair, $\sqrt{s_{\rm NN}}$ [GeV], the center-of-momentum rapidity and the centrality of the reaction considered. The λ_s values marked with a * are the result of a strangeness conservation constraint.

E [AGeV]	11.6	20	30	40	80	158
$\sqrt{s_{\rm NN}}$ [GeV]	4.84	6.26	7.61	8.76	12.32	17.27
$y_{\rm CM}$	1.6	1.88	2.08	2.22	2.57	2.91
$N_{4\pi}$ centrality	most central	7%	7%	7%	7%	5%
$R = p/\pi^+$, $N_{\rm W}$	$R = 1.23 \pm 0.13$	349 ± 6	349 ± 6	349 ± 6	349 ± 6	362 ± 6
Q/b	0.39 ± 0.02	0.394 ± 0.02	0.394 ± 0.02	0.394 ± 0.02	0.394 ± 0.02	0.39 ± 0.02
π^+	133.7 ± 9.9	184.5 ± 13.6	239 ± 17.7	293 ± 18	446 ± 27	619 ± 48
$R = \pi^-/\pi^+$, π^-	$R = 1.23 \pm 0.07$	217.5 ± 15.6	275 ± 19.7	322 ± 19	474 ± 28	639 ± 48
$R = K^+/K^-$, K^+	$R = 5.23 \pm 0.5$	40 ± 2.8	55.3 ± 4.4	59.1 ± 4.9	76.9 ± 6	103 ± 10
K^-	3.76 ± 0.47	10.4 ± 0.62	16.1 ± 1	19.2 ± 1.5	32.4 ± 2.2	51.9 ± 4.9
$R = \phi/K^+$, ϕ	$R = 0.025 \pm 0.006$	1.91 ± 0.45	1.65 ± 0.5	2.5 ± 0.25	4.58 ± 0.2	7.6 ± 1.1
Λ	18.1 ± 1.9	28 ± 1.5	41.9 ± 6.1	43.0 ± 5.3	44.7 ± 6.0	44.9 ± 8.9
$\overline{\Lambda}$	0.017 ± 0.005	0.16 ± 0.03	0.50 ± 0.04	0.66 ± 0.1	2.02 ± 0.45	3.68 ± 0.55
Ξ^-		1.5 ± 0.13	2.48 ± 0.19	2.41 ± 0.39	3.8 ± 0.260	4.5 ± 0.20
$\overline{\Xi}^+$			0.12 ± 0.06	0.13 ± 0.04	0.58 ± 0.13	0.83 ± 0.04
$\Omega + \overline{\Omega}$				0.14 ± 0.07		
$K_{\rm S}$						81 ± 4
V [fm^3]	3596 ± 331	4519 ± 261	1894 ± 409	1879 ± 183	2102 ± 53	3004 ± 1
T [MeV]	157.8 ± 0.7	153.4 ± 1.6	123.5 ± 3	129.5 ± 3.4	136.4 ± 0.1	136.4 ± 0.1
λ_q	5.23 ± 0.07	3.49 ± 0.08	2.82 ± 0.08	2.42 ± 0.10	1.94 ± 0.01	1.74 ± 0.02
λ_s	1.657^*	1.41^*	1.36^*	1.30^*	1.22^*	1.16^*
γ_q	0.335 ± 0.006	0.48 ± 0.05	1.66 ± 0.10	1.64 ± 0.04	1.64 ± 0.01	1.64 ± 0.001
γ_s	0.190 ± 0.009	0.38 ± 0.05	1.84 ± 0.32	1.54 ± 0.15	1.54 ± 0.05	1.61 ± 0.02
λ_{I3}	0.877 ± 0.116	0.863 ± 0.08	0.939 ± 0.023	0.951 ± 0.008	0.973 ± 0.002	0.975 ± 0.004
$\mu_{\rm B}$ [MeV]	783	576	384	344	271	227
$\mu_{\rm S}$ [MeV]	188	139	90.4	80.8	63.1	55.9

dent to not include its study here. The experimental yields of Ω and $\overline{\Omega}$ at 158 AGeV are contrary to the $\Lambda(1520)$ larger than the SHM model predicts. These particles are produced very rarely and for this reason any novel mechanism of production [22] would be first visible in their yield. We believe that it is also prudent to not include these in the study, even if the deviation from fit would be at 2 s.d. level.

2.2 AGS and SPS energy range fit

To assure the reproducibility of our analysis, we will describe in detail the input particle yields that are used, for the AGS/SPS energy domain, and for the RHIC domain in the next subsection. The set of particles available at AGS arises from several experiments, we have previously reported in detail the SHM analysis at the top AGS energy [23], whose input and fit results are restated here.

The study of AGS results was performed in [23] for several possible cases, such as with and without ϕ/K yield, strangeness (non)conservation. The results here presented are for the case in which the ϕ/K yield is fitted and strangeness is conserved. Differences in theoretical fit detail yield similar fit result which show the robustness of the approach.

For this work, the analysis of the $N_{4\pi}$ particle yields of the NA49 experimental group available at 20, 30, 40, 80 and 158 AGeV [24] has been carried out. This work extends significantly our prior study of the 40, 80 and 158 AGeV NA49 done when many fewer measurements were available [52]. Moreover, the SHARE package used offers additional theoretical features which were not fully implemented earlier: the consistent description of the yields of different charges hadrons (*e.g.*, protons and neutrons, π^+ and π^-) by means of λ_{I3} allows to fix the net charge fraction Q/b. The most relevant difference to the earlier study is, however, that we can address the two newly measured reaction energies, 20, 30 AGeV. This, along with the AGS 11.6 AGeV data, including the recently published ϕ yield [53], allows to recognize a major change in the behavior of the hadronizing fireball [2].

The input data we considered for the AGS and SPS are presented in top part of table 1. The statistical parameters are seen below these input data. In carrying out the data analysis, we use the full grand-canonical statistical set of

seven parameters: volume V, freeze-out temperature T, chemical quark fugacities $\lambda_{q,s}$, quark occupancy parameters γ_q and γ_s, and third component of the isospin fugacity λ_{I3}. The fitted values of these 7 parameters are seen near the bottom of table 1, which is followed by entries for the central values of the two chemical potentials:

$$\mu_{\rm B} = 3T \ln \lambda_q \,, \tag{1}$$
$$\mu_{\rm S} = \mu_{\rm B}/3 - T \ln \lambda_s \,. \tag{2}$$

The uncertainties in the value of statistical parameters comprise the propagation of the experimental measurement error through the fit, as well as the ambiguity due to statistical parameter correlations arising. In some instances this effect is very small, in others rather large. This wide disparity is possible, as sometimes the data set is sufficiently constraining, and in others it is not. The most interesting result, we notice in table 1, is the sudden shift in the values of the phase space occupancies γ_q and γ_s observed as reaction energy rises from 20 to 30 AGeV. The value of the chemical freeze-out temperature T changes accordingly to counterbalance the effect of a rapid change in γ_q and γ_s on some particle multiplicities. We will discuss this change in behavior in great detail in what follows. The steady decrease of the baryochemical potential $\mu_{\rm B}$ with the reaction energy follows the enhancement in the global yield of hadrons. At central rapidity the steady increase of baryon transparency with increasing collision energy yields a smaller value of $\mu_{\rm B}$. The total particle yields we consider here render an average over the entire rapidity range of $\mu_{\rm B}$. The associated value of $\mu_{\rm S}$ is controlled by the strangeness conservation condition, as discussed.

Excluding from the count of parameters λ_s, which is related to (near) strangeness conservation, there are 6 parameters, while there are between 9 and 12 data inputs at each energy considered in table 1. We thus have 3–6 degrees of freedom (d.o.f) for the fits carried out at AGS and SPS. Not all of the NA49 SPS energy range results we use are published in final form.

We show, in fig. 1, the reliability of the fits we obtained at different reaction energies as a function of γ_q, the light quark phase space occupancy. The results for AGS and SPS are accompanied by those for central rapidity RHIC fits we will address below. The top frame, in fig. 1, shows χ^2/dof. The associated significance level P [%] is seen in the bottom frame. We include P [%] as result, since the number of degrees of freedom in each fit is small and it is hard to judge the significance of a small value of χ^2/dof.

We study the dependence of χ^2/dof and P [%] on γ_q since we see, in table 1, that the two parameters which undergo a rapid change as a function of the reaction energy are γ_q, and to a lesser degree, the freeze-out temperature T. The rapid change with γ_q is prominent in fig. 1 where P [%] peaks for the lowest two energies (11.6 and 20 AGeV) at $\gamma_q < 0.5$, while for all other collision energies it grows to a maximum value near $\gamma_q \simeq 1.6$, where the Bose singularity of the pion momentum distribution $\gamma_q \simeq e^{m_\pi/T}$.

The reader can see, in fig. 1, that setting the value $\gamma_q = 1$ will yield a set of energy-dependent *individual* fits

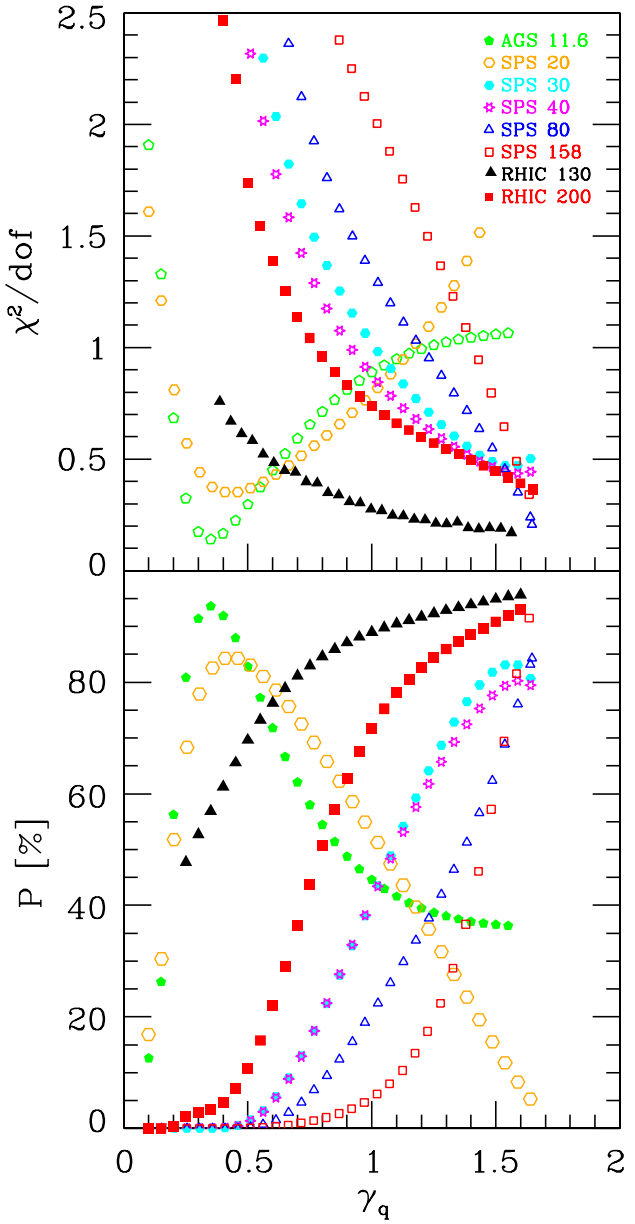

Fig. 1. χ^2/dof (top) and the associated significance level P [%] (bottom) as a function of γ_q, the light quark phase space occupancy. For the AGS/SPS energy range and for the (central rapidity) RHIC results.

which appear to have a good confidence level. However, the energy dependence of the particle yields derived at this fixed $\gamma_q = 1$ condition is less convincing. It is the rapid shift in the best γ_q as a function of the reaction energy which allows to describe the "horn" feature in the K^+/π^+ data (see fig. 2 below). Without the variable γ_i this horn feature is largely erased, see, *e.g.*, fig. 4 in [54], and the dashed and dotted lines in fig. 2. We will return to describe this effect in sect. 2.4, and discuss this physics in more detail in sect. 4.1. We believe that, in the study of energy-dependent particle yields, the use of the highest confidence level SHM results with $\gamma_q \neq 1$ is required for the description of energy-dependent particle yield data.

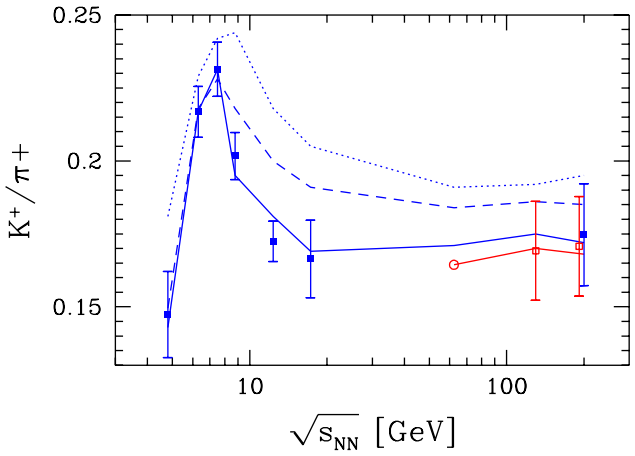

Fig. 2. (Colour on-line) K^+/π^+ total yields (filled squares, blue) and central rapidity density (open squares, red) as a function of $\sqrt{s_{\rm NN}}$. The solid lines show the chemical non-equilibrium model fit. The chemical equilibrium fit result is shown by the dotted line. The dashed line arises finding the best γ_s for $\gamma_q = 1$. See the text about the total yield results at $\sqrt{s_{\rm NN}} = 62.4$ and 130 GeV (unmarked edges in lines) and about the central rapidity yield at $\sqrt{s_{\rm NN}} = 62.4$ (open circle).

Regarding the weak decay (WD) contributions: in the fits to experimental data, we have followed the corrections applied to the data by the experimental group(s). For 20 and 30 GeV in Λ and $\overline{\Lambda}$ yields, the data we use includes the WD of Ξ, $\overline{\Xi}$, Ω and $\overline{\Omega}$, these matter mainly in consideration of antihyperon yields. At all higher SPS energies all hyperon WD decays are corrected for by the NA49 Collaboration, the $\Sigma^{\pm}$ decays are always corrected. Similarly, decays of kaons into pions are corrected for at all SPS energies. At AGS 11 GeV, all yields we consider are without WD contribution. The contamination of Λ by hyperons decays is not material. However, the decays of anti-hyperons contaminates in a highly relevant way the yields of $\bar{p}$ and we do not discuss here this effect further, the reader will note the relevant yields of $\bar{p}$, $\overline{\Lambda}$ and $\overline{\Xi}$ in table 2. The observable yield of $\bar{p}$ is further contaminated by decays of $\overline{\Sigma}^+$.

The model yields obtained are shown in table 2. These results are prior to any WD contributions. The yields of input particles can be compared to the fitted inputs seen in table 1. We present also predictions for yields of a number of other particles of interest. We do not show the uncertainty in these results, which can be considerable: in addition to the error propagating through the fit, there is a systematic error due to the shape of the χ^2/d.o.f. minimum, see fig. 1.

2.3 RHIC energy range fit

The RHIC central rapidity particle yields at $\sqrt{s_{\rm NN}} = 200$ and 130 GeV are analyzed using nearly the same method and principles described in the study of the total particle yields. This can be done for the case that the particle yields, and hence their source, is subject to (approximate)

Table 2. Output total hadron multiplicity data for AGS (left) and SPS (right). Additional significant digits are presented in particle yields for purposes of tests and verification. The SHM parameters generating these multiplicities are the central fit values seen in table 1. Hadron yields presented are prior to weak decays and apply to the total multiplicities $N_{4\pi}$ expected at the most central collision bin with the corresponding baryon content b as shown.

E [AGeV]	11.6	20	30	40	80	158
$\sqrt{s_{\rm NN}}$ [GeV]	4.84	6.26	7.61	8.76	12.32	17.27
$y_{\rm CM}$	1.6	1.88	2.08	2.22	2.57	2.91
$N_{4\pi}$ centrality	m.c.	7%	7%	7%	7%	5%
$b \equiv B - \overline{B}$	375.6	347.9	349.2	349.9	350.3	362.0
π^+	135.2	181.5	238.7	290.0	424.5	585.2
π^-	162.1	218.9	278.1	326.0	461.3	643.9
K^+	17.2	39.4	55.2	56.7	77.1	109.7
K^-	3.58	10.4	15.7	19.6	35.1	54.1
$K_{\rm S}$	10.7	25.5	35.5	37.9	55.1	80.2
ϕ	0.46	1.86	2.28	2.57	4.63	7.25
p	174.6	161.6	166.2	138.8	138.8	144.3
$\bar{p}$	0.021	0.213	0.68	0.76	2.78	5.46
Λ	18.2	29.7	39.4	34.9	42.2	48.3
$\overline{\Lambda}$	0.016	0.16	0.51	0.63	2.06	4.03
Ξ^-	0.47	1.37	2.44	2.43	3.56	4.49
$\overline{\Xi}^+$	0.0026	0.027	0.089	0.143	0.42	0.82
Ω	0.013	0.068	0.14	0.144	0.27	0.38
$\overline{\Omega}$	0.0008	0.0086	0.022	0.030	0.083	0.16
$K^0(892)$	5.42	13.7	11.03	12.4	18.7	19.1
Δ^0	38.7	33.43	25.02	26.6	27.2	28.2
Δ^{++}	30.6	25.62	22.22	24.2	25.9	26.9
$\Lambda(1520)$	1.36	2.06	1.73	1.96	2.62	2.99
$\Sigma^-(1385)$	2.51	3.99	4.08	4.26	5.24	5.98
$\Xi^0(1530)$	0.16	0.44	0.69	0.73	1.14	1.44
η	8.70	16.7	19.9	24.1	38.0	55.2
η'	0.44	1.14	1.10	1.41	2.52	3.76
ρ^0	12.0	19.4	14.0	18.4	32.1	42.3
$\omega(782)$	6.10	13.0	10.8	15.7	27.0	38.5
$f_0(980)$	0.56	1.18	0.83	1.27	2.27	3.26
$(s-\bar{s})/(s+\bar{s})$	0	−0.092	−0.085	−0.056	−0.029	−0.056

scaling, that means is flat as a function of the rapidity distribution [55]. The overall normalization of yields then contains, instead of the volume V, the volume fraction $\mathrm{d}V/\mathrm{d}y$ associated with the size of the volume at the rapidity of the source of particles at y. We note that, in the local rest frame, the total yield of particles $N_{4\pi}$ can be written in the equivalent forms:

$$N_{4\pi} = \int \mathrm{d}V\rho = \int \mathrm{d}y \frac{\mathrm{d}V}{\mathrm{d}y}\rho = \int \mathrm{d}y \frac{\mathrm{d}N}{\mathrm{d}y}. \qquad (3)$$

The local rest frame particle density, $\rho = \mathrm{d}N/\mathrm{d}V$, is thus related to the rapidity density by

$$\frac{\mathrm{d}N}{\mathrm{d}y} = \frac{\mathrm{d}V}{\mathrm{d}y}\rho. \qquad (4)$$

Table 3. The input particle data (top) and the resulting statistical parameters, and the chemical potentials derived from these, at bottom, for the RHIC energy range. Any of the entries with a * is set as input or is a constraint, *e.g.*, in general λ_s results from the constraint to zero strangeness. † indicates input particle multiplicity derived from interpolating yields between different energies, see the RHIC $\sqrt{s_{\rm NN}} = 62.4\,{\rm GeV}$ case. On the right, the case of central rapidity yields $\mathrm{d}N/\mathrm{d}y$, and on left, the total particle yields, in all cases considered for the most central 7% collisions. For $N_{4\pi}$, we show the participant count.

$\sqrt{s_{\rm NN}}$ [GeV]	62.4	130	200	62.4	130	200
$E_{\rm eq}$ [AGeV]	2075	9008	21321	2075	9008	21321
Δy	±4.2	±4.93	±5.36	±4.2	±4.93	±5.36
	$N_{4\pi}$ 5%			$\mathrm{d}N/\mathrm{d}y\|_{y=0}$ 5%		
$N_{\rm W}$	349 ± 6	349 ± 6	349 ± 6			
Q/b	0.39 ± 0.02	0.39 ± 0.02	0.39 ± 0.02	0.39 ± 0.02	0.4 ± 0.01	0.4 ± 0.01
π^-/π^+				1.02 ± 0.03	1.0 ± 0.03	1.0 ± 0.05
π^+	†1140 ± 90	†1450 ± 90	1677 ± 150		276 ± 36	286.4 ± 24.2
π^-			1695 ± 150		270 ± 36	281.8 ± 22.8
K^+			293 ± 26		46.7 ± 8	48.9 ± 6.3
K^-			243 ± 22		40.5 ± 7	45.7 ± 5.2
ϕ/K^-					0.15 ± 0.03	0.16 ± 0.03
p					28.7 ± 4	18.3 ± 2.6
$\bar{p}$					20.1 ± 2.8	13.5 ± 1.8
Λ				†17 ± 2	17.35 ± 0.8	
$\overline{\Lambda}$				†10 ± 1	12.5 ± 0.8	
Ξ^-/h^-					0.0077 ± 0.0016	
Ξ^-, Ξ^-/Λ				†2.05 ± 0.2	0.187 ± 0.046	2.17 ± 0.25
$\overline{\Xi}^+$, $\overline{\Xi}^+/\overline{\Lambda}$				†1.3 ± 1	0.215 ± 0.054	1.83 ± 0.25
$\overline{\Xi}^+/\Xi^-$					0.853 ± 0.1	
Ω/h^-					0.0012 ± 0.0005	
$(\Omega + \overline{\Omega})/h^-$					0.0021 ± 0.0008	
$K^0(892)/K^-$					0.26 ± 0.08	0.23 ± 0.05
V, $\mathrm{d}V/\mathrm{d}y$ [fm^3]	4871 ± 394	6082 ± 384	8204 ± 351	932 ± 38	930 ± 3	1182 ± 55
T [MeV]	140*	141.9 ± 0.5	142.4 ± 0.01	142.2 ± 0.01	143.8 ± 0.1	141.5 ± 0.1
λ_q	1.35 ± 0.02	1.25 ± 0.01	1.20 ± 0.01	1.15 ± 0.02	1.076 ± 0.001	1.062 ± 0.001
λ_s	1.104*	1.074*	1.069*	1.054*	1.025*	1.024*
γ_q	1.62*	1.62*	1.62*	1.62*	1.59 ± 0.001	1.56 ± 0.01
γ_s	2.18 ± 0.2	2.20*	2.00 ± 0.29	2.13 ± 0.14	2.22 ± 0.01	2.00 ± 0.02
λ_{I3}	0.933 ± 0.001	0.979 ± 0.001	0.988 ± 0.002	0.986 ± 0.002	0.997 ± 0.001	0.997 ± 0.001
$\mu_{\rm B}$ [MeV]	126	94.8	79	61.2	31.5	25.7
$\mu_{\rm S}$ [MeV]	27.7	21.4	16.5	13.6	7.0	5.2

The SHM fits to particle densities $\mathrm{d}N/\mathrm{d}y$ thus produce as the normalization factor the value $\mathrm{d}V/\mathrm{d}y$. The qualitative relation between $\mathrm{d}V/\mathrm{d}y$ and V (rest frame hadronization volume) must include the maximum rapidity range $2y_p$, where y_p is the rapidity of the nuclei colliding head on

$$V = k\frac{\mathrm{d}V}{\mathrm{d}y} \times 2y_p\,, \tag{5}$$

where k is a reaction energy-dependent constant. The study of the total hadron yields at RHIC we present suggests $k \simeq 0.4$–0.6.

Regarding the data source, and weak decay acceptance, we need to consider case by case the experimental results, since the relative importance of hyperon decays in the total baryon yields is high. In particular, we note:

– For RHIC-130 $\mathrm{d}N/\mathrm{d}y$ fit (second column from the right in the top section of table 3):
The $\pi^\pm$, $K^\pm$, p and $\bar{p}$ 5% centrality results are from PHENIX [56]. We assume that the $K_{\rm S}$ decays into pions are accepted at 70% level, and $K_{\rm L}$ at 40% level. Mesons (pions and kaons) from hyperon decays are accepted at 30% level, while nucleons from hyperon de-

cay are nearly fully accepted, both 90% and 99% acceptances are in essence indistinguishable. $\Sigma^{\pm}$ decays are fully accepted. We include in the fit an average of the STAR [57] and PHENIX [58] Λ and $\overline{\Lambda}$ yields where we can asses the feed from Ξ and $\overline{\Xi}$ in view of the STAR analysis [59], we accept 99% of Ω and $\overline{\Omega}$ decays into Λ and $\overline{\Lambda}$.

For the Ξ and $\overline{\Xi}$ weak feed yield corrections are immaterial. However, we cannot directly use the yields as these are presented for the 10% most central reactions. We fit the weak decay corrected Ξ/Λ and $\overline{\Xi}/\overline{\Lambda}$ ratios. In order to relate this to the total particle yields, we include also Ξ/h^- (h^- = negatives) where we accept in STAR h^- the weak decay products according to the pattern: $K_{\rm S}$ decays into pions are accepted at 90% level, and $K_{\rm L}$ at 30% level, pions and kaons from hyperon decays are accepted at 50% level, while nucleons from hyperon decay are accepted, at 99% level. The same is assumed in the fit of $(\Omega+\overline{\Omega})/h^-$ also measured by STAR [59]. We include in the fit the STAR resonance ratios, $K^0(892)/K^-$ [60] and ϕ/K^- [61], in both cases we include 50% feed from Ω and $\overline{\Omega}$ decay into kaons, which is immaterial for the result.

– For RHIC-200: dN/dy fit (last column on the right in the top section of table 3):

The $\pi^{\pm}$, $K^{\pm}$, p and $\bar{p}$ 5% centrality results are from PHENIX [62]. We assume that the $K_{\rm S}$ weak decays are accepted at 70% level, and $K_{\rm L}$ at 40% level. Mesons (pions and kaons) from hyperon decays are accepted at 30% level, while nucleons from hyperon decay are nearly fully accepted, we included this at 90% level in the reported fit. $\Sigma^{\pm}$ decays are fully accepted. We take the STAR resonance ratios, $K^0(892)/K^-$ [63,64] and ϕ/K^- [65], in both cases we include 50% feed from Ω and $\overline{\Omega}$ decay into kaons. The method to study the yields of stable hadrons along with resonances follows the work on the impact parameter dependence at $\sqrt{s_{\rm NN}} = 200\,{\rm GeV}$ [3].

We did not use yields of Λ and $\overline{\Lambda}$ since without direct measurement of Ξ and $\overline{\Xi}$ it is hard to judge the weak decay contamination in the data. Furthermore, we preferred to study the relative yields p/π^+, $\bar{p}/\pi^-$. In the fit presented, we assumed that the pion feed from WD of hyperons is at 80% level. The other WD characteristics are as discussed just above. This slight change in the data input and also the slight modification of the pattern of weak decay acceptance has, in comparison to ref. [3], yielded an increase of the volume factor dV/dN by 1.2 s.d., while other variations are within 0.5 s.d.

We can expect, in the near future, particle multiplicity results from RHIC obtained at $\sqrt{s_{\rm NN}} = 62.4\,{\rm GeV}$. We interpolate the central rapidity yields of strange hyperons Λ, $\overline{\Lambda}$, Ξ and $\overline{\Xi}$, presented in [66], to this energy. With these 4 inputs, two constraints, setting the $\gamma_q = 1.62$, $T = 140$, we find a good description of the interpolated data but with a few degrees of freedom. We have four interpolated "data" points, two constraints —strangeness conservation and Q/b, thus 6 data points which are fitted using four flexible parameters, T, dV/dN, λ_q, and λ_{I3}. This set of parameters, then, yields our prediction of central rapidity particle multiplicities, seen in table 4, for $\sqrt{s_{\rm NN}} = 62.4\,{\rm GeV}$.

Table 4. Output hadron multiplicity data for the RHIC energy range. See the text for the meaning of predictions of $N_{4\pi}$ yields at 62.4 and 130 GeV and of dN/dy at 62.4 GeV. The input statistical parameters are seen in table 3. $b = B - \overline{B} \equiv N_{\rm W}$ for 4π results and $b = {\rm d}(B - \overline{B})/{\rm d}N$ for results at central rapidity. Additional significant digits are presented for purposes of tests and verification. All yields are without the weak decay contributions.

$\sqrt{s_{\rm NN}}$ [GeV]	62.4	130	200	62.4	130	200
$E_{\rm eq}$ [GeV]	2075	9008	21321	2075	9008	21321
Δy	±4.2	±4.93	±5.36	±4.2	±4.93	±5.36
	$N_{4\pi}$ 5%			${\rm d}N/{\rm d}y\|_{y=0}$ 5%		
b	350.2	350.2	349.6	33.48	18.50	14.8
π^+	899	1201	1543	183.8	230.3	239.8
π^-	927	1229	1573	186.7	231.9	241.0
K^+	230.9	302.5	291.9	43.7	47.9	47.1
K^-	168.5	238.4	242.3	37,6	44.2	44.2
$K_{\rm S}$	193.8	261.0	259.9	39.4	44.4	44.2
ϕ	27.3	34.6	28.9	5.74	6.86	6.18
p	140.0	157.6	192.0	19.34	17.09	16.34
$\bar{p}$	24.1	42.9	66.1	8.37	11.11	11.44
Λ	81.1	97.4	89.9	12.3	12.04	10.7
$\overline{\Lambda}$	20.2	35.1	38.3	6.36	8.60	8.02
Ξ^-	12.9	16.4	11.6	2.14	2.30	1.91
$\overline{\Xi}^+$	4.6	7.79	6.13	1.32	1.80	1.53
Ω	1.94	2.68	1.45	0.36	0.44	0.33
$\overline{\Omega}$	1.04	1.74	0.98	0.27	0.38	0.29
$K^0(892)$	48.7	67.4	68.1	10.2	11.5	11.2
Δ^0	27.6	31.1	38.1	3.78	3.32	3.15
Δ^{++}	26.2	29.9	36.9	3.69	3.30	3.13
$\Lambda(1520)$	4.43	6.4	6.0	0.81	0.81	0.70
$\Sigma^+(1385)$	9.80	11.91	11.19	1.52	1.50	1.33
$\Xi 0(1530)$	4.20	5.46	3.88	0.71	0.78	0.64
η	131.9	179.5	192.3	27.2	30.5	30.6
η'	10.8	15.2	14.64	2.30	2.64	2.51
ρ^0	85.8	117	157	18.1	19.5	20.3
$\omega(782)$	75.9	104	142.8	16.2	17.4	18.3
$f_0(980)$	6.51	9.03	12.96	1.40	2.02	1.58
$(s-\bar{s})/(s+\bar{s})$	0	0	0	0	0	0

We make an effort to understand also the recently finalized total multiplicities $N_{4\pi}$ of $K^{\pm}$ and $\pi^{\pm}$ [67] at $\sqrt{s_{\rm NN}} = 200\,{\rm GeV}$. Additional qualitative constraint is derived from total charge particle multiplicities [68], however this result is not used directly in the fit. With the three constraints, four BRAHMS particle yields, we have 7 data points, and also 7 SHM parameters. To be able to make a fit with at least one degree of freedom it is necessary to make some "natural" hypothesis.

We choose to consider $\gamma_q = 1.62 \simeq e^{m_\pi/2T}$, which we find systematically at the RHIC energy scale. Our "fit" to $N_{4\pi}$ data at $\sqrt{s_{\rm NN}} = 200\,{\rm GeV}$ works, but it must not be seen as a full fit, rather a consistency test of SHM. This is allowing a prediction to be made of other $N_{4\pi}$ shown in table 4. This consideration is also yielding a rapidity-averaged value of T and of the 5 chemical parameters, as well as an estimate of the proper size V of the hadronizing fireball. The value of $\mu_{\rm B}$, which varies as a function of rapidity, following the highly variable baryon distribution [69], is found at a median value, seen at the bottom of table 3, on the left for the $N_{4\pi}$ fits.

We extend the consideration of the $N_{4\pi}$ yields to the lower energies, $\sqrt{s_{\rm NN}} = 62.4$ and $130\,{\rm GeV}$. This can be done assuming that there is no change in physics between top SPS energy and RHIC 200 GeV run. Thus, the success of our particle yield prediction would be a confirmation of this hypothesis. Our procedure can be seen in detail on the left of table 3. We fix the hadronization temperature at $T = 140\,{\rm MeV}$, choose the value $\gamma_q = 1.62 \simeq e^{m_\pi/2T}$, and interpolate the values of γ_s. We do find the required values of λ_q, λ_{I3} and V needed to assure the total baryon yield, fraction of charge Q/b and one particle yield, which we choose to be the interpolated total π^+. We use the observation that the π^+ yield from Brahms connects, in a logarithmic plot, in a nearly perfect straight line with the SPS energy domain. This produces the π^+ interpolated values we introduced in table 3. The SHM succeeds perfectly and allows us to offer predictions for the total particle yields presented in table 4.

We present, in detail, the resulting particle multiplicities in table 4 for RHIC. On left, we show the expected total yields and on right the central rapidity yields. We recall that, among total yields, only at 200 GeV a significant experimental input was available, thus the 62.4 and 130 GeV total yield results are an educated guess satisfying all constraints and criteria of the SHM model. Similarly, the central rapidity region yields for 62.4 GeV is a prediction based on interpolated yields, with inputs seen in table 3. All results, presented in table 4, are obtained prior to WD.

2.4 Energy-dependent particle yields

We consider, more systematically, the energy dependence of particle yields and ratios. Of particular interest is the ratio K^+/π^+ which shows the previously unexplained horn structure. We compare the experimental and theoretical behavior in fig. 2. The 4π results are blue filled squares. The central rapidity RHIC results (on the right in red) are shown as open squares, while the predicted total yield ratio for $\sqrt{s_{\rm NN}} = 62.4$ is given as an open circle.

We recall that the abrupt increase in the value of γ_q occurs where the rise in K^+/π^+ reverses, turning into a sudden decrease with reaction energy. The solid line, shows our chemical non-equilibrium fit which reproduces the horn structure well. The predicted total yield ratios for $\sqrt{s_{\rm NN}} = 62.4$ and 130 GeV (edges in solid line) arise from the interpolation of yields and/or continuity in the value of statistical parameters such as γ_q between the top SPS and the top RHIC energy, see above, sect. 2.3.

The dotted line, in fig. 2, presents best fit results obtained within the chemical equilibrium model, *i.e.*, with $\gamma_s = \gamma_q = 1$, using the same computer program (SHARE), and the same data set. We see that the chemical equilibrium SHM cannot explain the horn in the K^+/π^+ ratio. The dashed line corresponds to the result obtained fixing $\gamma_q = 1$ but allowing γ_s to assume a best value. We see that, without $\gamma_q > 1$, it is difficult, if not impossible, to obtain the large reduction of the K^+/π^+ ratio with increasing energy. These findings are in line with prior attempts to explain the horn structure, see, *e.g.*, fig. 4 in [54]. We note that our semi-equilibrium results follow better the trend set by the experimental data, which is a consequence of the relaxation of the exact strangeness conservation requirement. It appears that the full chemical non-equilibrium statistical hadronization model is required in order to obtain a satisfactory understanding of the energy dependence of the K^+/π^+ ratio.

A graphic comparison of the experimental input, and theoretical output particle yields as a function of energy for several other particles is seen in fig. 3. We show K^-/π^- with Λ/π^+, Ξ^-/π^- with $5\,\Omega^-/\pi^-$, $\overline{\Xi}^+/\overline{\Lambda}$ with $2\,\overline{\Omega}/\overline{\Xi}^+$ and at bottom $\phi/\sqrt{\pi^+\pi^-}$. We are showing the total SHM yield ratios at AGS/SPS as well as at RHIC, connected by a solid line (thick and/or thin). The central rapidity yields at RHIC are also presented for comparison by the dashed lines.

The SHM allowing for chemical non-equilibrium reproduces all salient features of the experimental particle yield data well as a function of energy, including the NA49 results that otherwise could not be described in equilibrium and semi-equilibrium approach [25], *e.g.*, the already discussed K^+/π^+ ratio shown in fig. 2. In addition, in fig. 3, we note in the top panel the shift of the s-quark population from its dominant baryon component (see Λ/π^+) at low reaction energy, to meson carriers (see K^-/π^-).

Of particular importance, in the study of quark-gluon plasma formation, is the strange antibaryon enhancement. It is one of the most important signatures of deconfinement [70]. These particles are hard to make in conventional environment, and are also highly sensitive probes of the medium from which they emerge. There is still only fragmentary data available for the antibaryon ratios of interest, $\overline{\Xi}^+/\overline{\Lambda}$ and $2\overline{\Omega}/\overline{\Xi}^+$, shown in fig. 3, in the third panel from the top.

In fig. 4, we show as a function of energy the individual yields of $\overline{\Lambda}$, $\overline{\Xi}^+$ and $\overline{\Omega}^+$, along with the experimental data used as input. All three antihyperon production rates are predicted to rise at nearly the same rate as a function of $\sqrt{s_{\rm NN}}$ —indeed the strange antibaryon ratios, we have shown in fig. 3, are as good as flat compared to the great variability of the absolute yields, which are increasing very rapidly, as is seen in fig. 4. The strange antibaryon production enhancement phenomenon has been considered in terms of a comparison of yields of antibaryons to a baseline yield obtained scaling the pp or pBe yields. This was

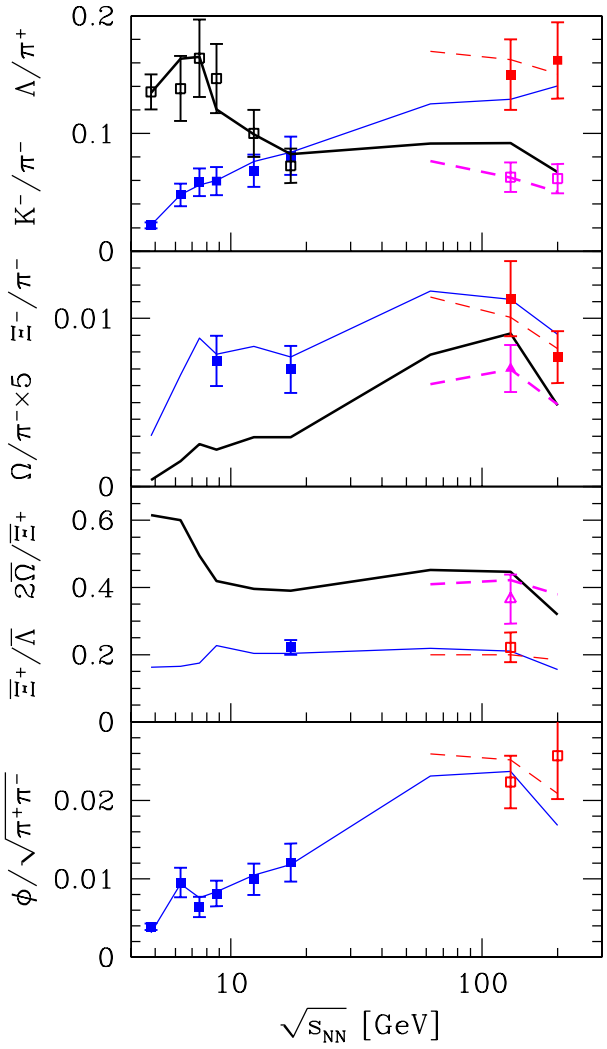

Fig. 3. (Colour on-line) Comparison of experimental and theoretical ratios of particle yields as a function of the reaction energy $\sqrt{s_{\rm NN}}$ —theoretical SHM total $N_{4\pi}$ results are connected by solid lines, with thick/thin lines corresponding to the different particle ratios. The (corresponding) dashed lines connect the central rapidity dN/dy results at RHIC. Experimental data used as fit input is shown with its error bar.

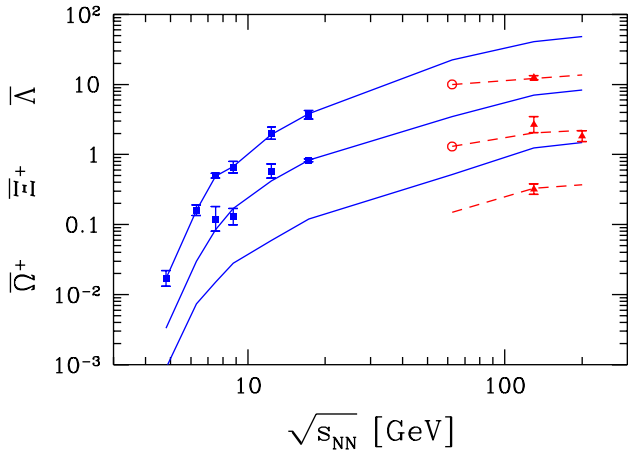

Fig. 4. (Colour on-line) Yields of strange antibaryons as a function of $\sqrt{s_{\rm NN}}$, from top to bottom $\overline{\Lambda}$, $\overline{\Xi}^+$ and $\overline{\Omega}^+$. The solid lines connect the results of SHM $N_{4\pi}$ fit to particle data. The AGS/SPS energy range $N_{4\pi}$ yields (in blue) on the left and RHIC $N_{4\pi}$ on the right. Also on the right (in red, connected with dashed lines) are the central dN/dy yields. The yields at $\sqrt{s_{\rm NN}} = 62.4$ used in our study are result of interpolation of RHIC and SPS results.

done as a function of the impact parameter, and reaction energy [71].

We note that the SHM non-equilibrium approach under-predicts by 1.5 s.d. the yields of Ω and $\overline{\Omega}$, for both SPS-NA49 results available at 40 and 158 AGeV. We did not include 158 AGeV results in our input data set since non-SHM source, such as chiral condensate [22], can generate such an excess.

Ratios of strange antibaryons are a sensitive probe of the medium. Once the deconfined phase is formed, the ratios of yields of strange antibaryons should not change drastically. Thus, our finding as a function of energy in essence of a flat ratio, with minor fluctuations originating in the other experimental data and amplified by the sensitivity of these particles, suggest that the same form of (deconfined) matter is present at SPS and RHIC, except perhaps for the lowest SPS reaction energy.

Another important point is that these antihyperon ratios are relatively large, and hard to understand except in terms of the quark coalescence picture. It would be very interesting to confirm experimentally that, at AGS energy scale, $2\overline{\Omega}/\overline{\Xi}^+$ is indeed as large as predicted in fig. 3. This would establish coalescence quark chemistry in this low-energy environment. Further, this maybe taken as an indication that the transition we observed at $\sqrt{s^{\rm cr}_{\rm NN}}$ involves two deconfined phases of different structure. We will further discuss this in sect. 4.

2.5 Yields of pentaquark hadrons

There are now more than 600 papers with the title word "pentaquark", however, on balance the evidence for the exotic hadrons $\Theta^+(1540)$ with the quark content $[uudd\bar{s}]$, and typical decays pK^0, nK^{*+}, and $\Xi^{--}(1862)[ssdd\bar{u}]$, with typical decays $\Xi^-\pi^-$, Σ^-K^-, is not convincing. The $\Xi^{--}(1862)$ may have been observed by NA49 in pp interactions at top SPS energy [72]. The $\Theta^+(1540)$ remains uncertain: several high-statistics confirmation experiments failed to find this state. Arguments were presented why these states were incorrectly identified [73]. We have therefore not included these and other related exotic quark states in the hadron resonance list in SHARE, when performing the fits here presented.

On the other hand, theoretical arguments for the existence of pentaquark states have not been refuted. We thus present in table 5 predictions for the production rates of Θ^+ and Ξ^{--}. These yields are highly sensitive to the hadronization conditions [74], and were obtained using the parameters of the fits here presented.

Table 5. Predicted yields of $\Theta^+(1540)$ and $\Xi^{--}(1820)$ pentaquarks for AGS, SPS and RHIC, obtained with the SHM parameters shown in tables 1 and 3.

E [AGeV]	11.6	20	30	40	80	158	2075	9008	21321
$\sqrt{s_{\rm NN}}$ [GeV]	4.84	6.26	7.61	8.76	12.32	17.27	62.4	130	200
$N_{4\pi}$ centrality	m.c.	7%	7%	7%	7%	5%	5%	5%	5%
$\Theta^+(1540)$	0.66	1.14	6.90	7.15	6.52	6.70	7.23	7.92	7.19
$\Xi^{--}(1820)$	0.0022	0.010	0.098	0.11	0.18	0.24	0.71	0.89	0.78

The expected statistical hadronization yield of Θ^+ rises rapidly, by an order of magnitude, between 11 and 30 AGeV reaction energies and remains practically constant thereafter. The expected $\Theta^+(1540)$ yield in fact exceeds the SHM predicted yield of $\Lambda(1520)$ in the threshold energy domain by a factor 2–4, and comparing to the observed $\Lambda(1520)$ yield at 158 AGeV by more than a factor 4. Furthermore, at 30 AGeV the background multiplicity is relatively small, while the rapidity range is also restricted compared to the top SPS energy, which should help finding the pentaquark, if it exists, in the range of energies characterizing the horn in the K^+/π^+.

3 Fireball properties at breakup

3.1 Energy dependence of model parameters

The statistical parameters of the SHM are shown, as a function of $\sqrt{s_{\rm NN}}$, in fig. 5, for the entire energy domain. From top to bottom, we see the chemical freeze-out temperature T, the statistical occupancy parameters γ_q and γ_s/γ_q and the chemical potentials $\mu_{\rm B}$ and $\mu_{\rm S}$. The error bars comprise the propagation of the experimental yield errors, as well as any uncertainty due to the shape of the χ^2/d.o.f. minimum, seen in fig. 1. The (red) triangle results are for the RHIC dN/dy case, while (blue) squares are for the $N_{4\pi}$ data throughout the energy domain and include the estimates we made for the RHIC energy range.

The only significant difference between RHIC dN/dy and $N_{4\pi}$ results is noted for the chemical potentials $\mu_{\rm B}$ and $\mu_{\rm S}$ and shown in the bottom panel (note the logarithmic scale). Across the entire energy range, the baryochemical potential $\mu_{\rm B}$ drops relatively smoothly as the reaction energy is increased. The vertical line indicates the observed sudden change in the structure of the fireball. This is seen in several statistical variables, but most clearly in γ_q.

It is important to recall that we present γ_i evaluated using hadronic multiplicities. If these arise from breakup of a quark fireball, the quark-side occupancy parameters could be considerably different. The hadron-side phase space size is, in general, different from the quark-side phase space, since the particle degeneracies, and masses, are quite different. In the study of the breakup of the quark fireball into hadrons, we can compute the resultant hadron phase space occupancy for two extreme limits.

First, consider a fast transformation (sudden breakup) of the quark phase. This occurs nearly at fixed volume. To accommodate the difference in the momentum part of the phase space, the chemical occupancy non-equilibrium parameters γ_i undergo an abrupt change. We note that it is of no importance if there was, or not, a phase transition between the phases, what matters is that there was no time to re-equilibrate chemically the quark yields. In the opposite limit of a very slow transformation of phases, there is available a prolonged period in time in which the volume of the system can change to accommodate the ap-

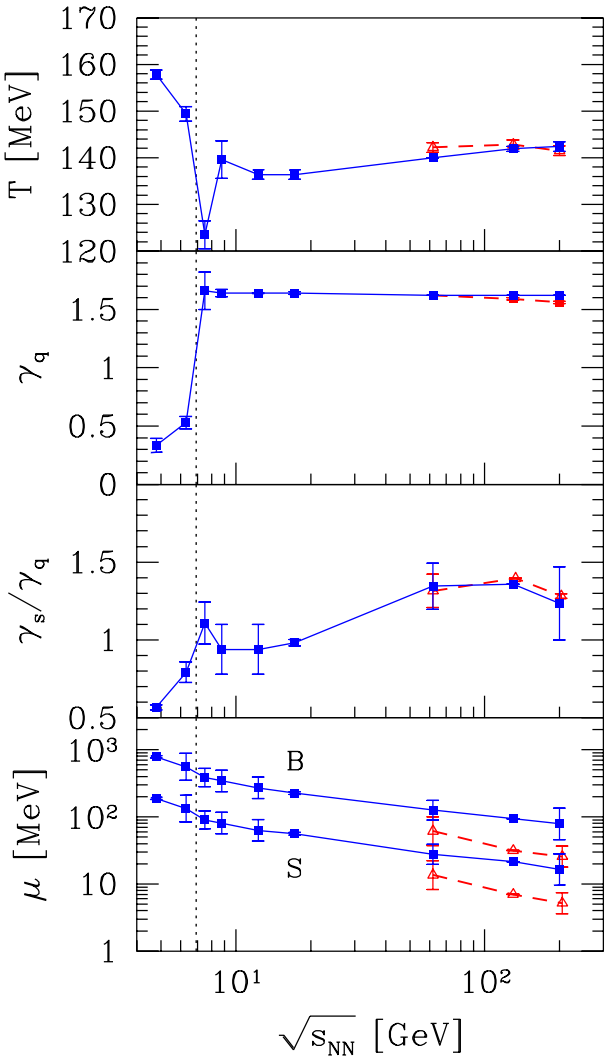

Fig. 5. (Colour on-line) Statistical parameter results for $N_{4\pi}$ (blue squares). From top to bottom: T, γ_q, γ_q/γ_s and $\mu_{\rm B}$, $\mu_{\rm S}$ [MeV], as a function of $\sqrt{s_{\rm NN}}$. The lines guide the eye. The same for dN/dy at RHIC (red triangles).

Table 6. The physical properties: pressure P, energy density $\epsilon = E_{\rm th}/V$, entropy density S/V, strangeness density s/V for AGS and CERN energy range at (top line) the projectile energy E [GeV]. Bottom: dimensionless ratios of properties at the fireball breakup, P/ϵ and $E_{\rm th}/TS$.

E [AGeV]	11.6	20	30	40	80	158
$\sqrt{s_{\rm NN}}$ [GeV]	4.84	6.26	7.61	8.76	12.32	17.27
P [MeV/fm^3]	21.9	21.3	58.4	68.0	82.3	76.9
ϵ [MeV/fm^3]	190.1	166.3	429.7	480.2	549.9	491.8
S/V [1/fm^3]	1.25	1.21	2.74	3.07	3.54	3.26
$100\bar{s}/V$ [1/fm^3]	0.988	1.52	5.32	5.85	7.65	7.24
ρ_b [1/fm^3]	0.104	0.0753	0.184	0.186	0.167	0.121
P/ϵ	0.115	0.128	0.136	0.142	0.150	0.156
$E_{\rm th}/TS$	0.96	0.92	1.27	1.20	1.14	1.11

propriate number of particles in chemical equilibrium corresponding to the maximum entropy content.

To determine the change in γ_i in sudden hadronization, one needs to compare in detail the phase space of quark phase with that of the hadron gas. In order to make this comparison, one must consider the energy and entropy content of the QGP phase. For $\mu_{\rm B} = 0$, as well as small chemical potentials $\mu_{\rm B}/T < 1$, lattice evaluation of the deconfined phase properties is available [75–78]. It is thus possible to model quantitatively the properties of the deconfined phase, and to compare these with the results of the SHM [79]. The remarkable result is that near to $T = 140\,{\rm MeV}$ the sudden transition requires the value $\gamma_q \simeq 1.6$ on the hadron side, if the quark phase was chemically equilibrated.

Thus, the large values of $\gamma_s^{\rm HG}$ and $\gamma_q^{\rm HG}$, seen in fig. 5 at large $\sqrt{s_{\rm NN}}$, where $\mu_{\rm B}/T < 1$ are consistent with the sudden breakup of the chemically equilibrated primordial QGP phase. Other dynamic effects, in particular, fast expansion, in general, also favor an over-saturated phase space with $\gamma_i > 1$.

As seen in fig. 5, γ_s/γ_q rises at first rapidly, as expected if strangeness production is delayed by a greater threshold mass and has to catch up with the light hadron production. γ_s/γ_q decreases beyond the edge of energy threshold, as can be expected due to the conversion of the quark to hadron occupancy discussed above. The rise resumes and continues for all energies above 80 AGeV.

3.2 Physical properties

We now turn our attention to the physical properties of the hadronizing fireball obtained summing individual properties of the hadronic particles produced. One can view the consideration of the physical properties of the fireball at breakup as another way to present the SHM parameters. For example, the net baryon density, $\rho_b \equiv (B - \overline{B})/V$, is most directly related to the baryochemical potential $\mu_{\rm B}$, the thermal energy density $E_{\rm th}/V$ is related to T etc.

We present the physical properties, *i.e.*, pressure P, energy density ϵ, entropy density S/V, net baryon density $\rho_b \equiv (B - \overline{B})/V$ and the yield of strangeness s, in table 6 for the AGS/SPS energy range considered. Note that s contains hidden strangeness from η, ϕ and η'. At the bottom of table 6, we show the dimensionless ratios of extensive variables P/ϵ, and $E_{\rm th}/TS$. These two ratios are very smooth as a function of energy, and lack any large fluctuations that could be associated with fit error. These ratios are characteristic for the conditions of the fireball at the point of hadronization.

Table 7. The physical properties for the RHIC energy range. For the central rapidity case, we show the rapidity densities: the energy rapidity density $\epsilon = {\rm d}E_{\rm th}/{\rm d}V$, the entropy rapidity density ${\rm d}S/{\rm d}V$, the strangeness rapidity density ${\rm d}s/{\rm d}V$ and the net baryon rapidity density ${\rm d}b/{\rm d}V$. The 62.4 GeV results, and the 130 GeV 4π result are, as discussed in text, result of assumptions, and/or interpolations of yields and/or parameters, and hence are a prediction.

$\sqrt{s_{\rm NN}}$ [GeV]	62.4	130	200	62.4	130	200
	$N_{4\pi}$			${\rm d}N/{\rm d}y\|_{y=0}$		
P [MeV/fm^3]	82.4	87.8	80.0	80.5	91.4	94.5
${\rm d}E_{\rm th}/{\rm d}V$ [MeV/fm^3]	516.6	548.4	478.9	532.5	604.4	479.4
${\rm d}S/{\rm d}V$ [1/fm^3]	3.62	3.73	3.32	3.64	4.03	3.32
$100{\rm d}\bar{s}/{\rm d}V$ [1/fm^3]	11.5	12.4	9.2	12.0	13.7	10.4
$100{\rm d}b/{\rm d}V$ [1/fm^3]	7.19	5.76	4.26	3.59	1.99	1.26
$P{\rm d}V/{\rm d}E_{\rm th}$	0.159	0.160	0.167	0.151	0.151	0.197
${\rm d}E_{\rm th}/T{\rm d}S$	1.02	1.04	1.01	1.03	1.04	1.02

The results presented can be used to constrain dynamical models describing the evolution of the QGP fireball in time towards hadronization/particle freeze-out. We present the energy range at RHIC on the left in table 7. We recall that the 62.4 GeV and the 130 GeV 4π results, as well as in part the 200 4π results, are the result of considerations which do not involve experimental measured particle yields. Thus, the 4π results are to be seen as a SHM prediction. On the right, in table 7, we present the results for central rapidity densities. Here, only the 62.4 GeV case is a prediction, the other results are a direct consequence of the data interpretation in terms of SHM.

The fit uncertainty in the quantities presented in tables 6 and 7 is difficult to evaluate in detail. The individual physical properties require powers and exponents of statistical parameters, and thus, at first sight, we expect that the fractional errors are increased, as compared to those prevailing among the statistical parameters in tables 1 and 3. However, the dominant contributions to each physical property is often directly derived from the individual observed particle yields. Therefore, a large compensation of errors originating in the fitted statistical parameter errors must occur.

For example, most of the pressure at breakup is due to the most mobile, lightest particle, the pion. These yields are known to better than 10%, and thus, the pressure must be known to greater precision since there are further constraints from consistency of this yield with the yield of other particles. This explains why the results when presented graphically (see fig. 6) are at 5% level smooth

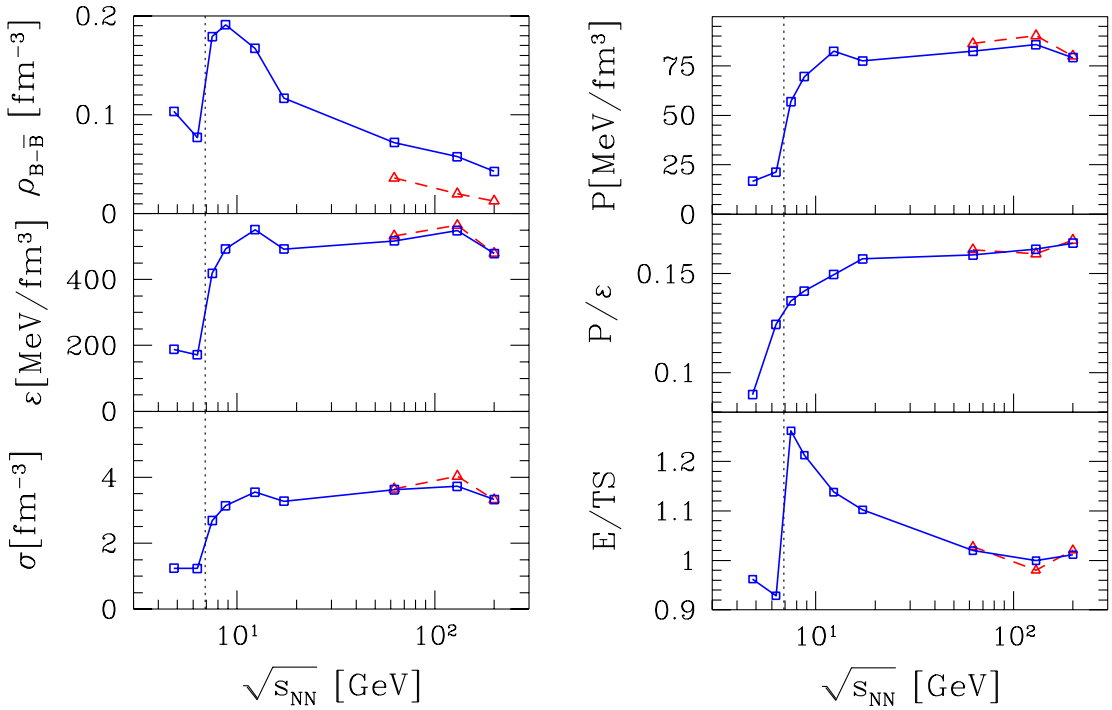

Fig. 6. (Colour on-line) From top to bottom, on the left-hand side the baryon density $\rho_{B-\overline{B}}$ [fm^{-3}], energy density ϵ [MeV/fm^3], and entropy density σ [fm^{-3}], as a function of $\sqrt{s_{\rm NN}}$, on the right-hand side the pressure P [MeV/fm^3], P/ϵ, and $E_{\rm th}/TS = \epsilon/T\sigma$. Squares (blue) average over the entire fireball at hadron freeze-out, triangles (red) for the central rapidity region of the fireball.

functions of $\sqrt{s_{\rm NN}}$, with fluctuations apparently at worse similar to those we see in the individual statistical SHM parameters. In the future, one could hope to fit the physical properties to the experimental data directly, bypassing the statistical parameters. This can be done, in principle, considering the mathematical properties of these expressions. However, such study transcends considerably the scope of this paper, and it is indeed motivated by the results we present for the first time here.

On the left-hand side, in fig. 6, we see from top to bottom the baryon density, the thermal energy density ϵ and the entropy density σ. On the right-hand side, from top to bottom, we show the pressure P, and the dimensionless ratio of pressure to thermal energy density P/ϵ, and $E_{\rm th}/TS = \epsilon/T\sigma$. The triangles (red) correspond to the properties of the fireball at central rapidity at RHIC energy scale. We note a significant difference between the total fireball averages (squares) and the central rapidity result (triangles) only in the net baryon number density.

As the reaction energy passes the threshold, $6.26\,{\rm GeV} < \sqrt{s^{\rm cr}_{\rm NN}} < 7.61\,{\rm GeV}$, the hadronizing fireball becomes much denser: the entropy density jumps by a factor 4, and the energy and baryon number density by a factor 2–3. The hadron pressure increases from $P = 25\,{\rm MeV/fm^3}$ initially by a factor 2, and ultimately more than a factor 3. There is a more gradual increase of $P/\epsilon = 0.115$ at low reaction energy to 0.165 at the top available energy.

For AGS 11 GeV and SPS 20 GeV results, the value $E/TS \simeq 0.9$. After a jump up at 30 AGev, there is monotonic fall, but $E/TS > 1$ as is expected for sudden hadronization, see sect. 4.5. We believe that any structure model of the phase transformation, and/or the two-phase structure will need to address E/TS, and/or P/ϵ freeze-out condition results quantitatively. These two ratios, $E_{\rm th}/TS$ and P/ϵ, are related. Restating the 1st law of thermodynamics

$$\frac{E_{\rm th}}{TS}(1+k) = 1 + \frac{\Sigma_i \nu_i \ln \Upsilon_i}{\sigma}\,, \quad k = \frac{P}{\epsilon}\,. \tag{6}$$

For each hadron fraction with density ν_i the total fugacity is

$$\Upsilon_i = \prod_j \gamma_j^{n_j} \lambda_j^{n_j}\,, \tag{7}$$

where all valence quarks and antiquarks of each hadron fraction contribute in the product, see sect. 2 in [14]. In the limit of chemical equilibrium:

$$\frac{\Sigma_i \nu_i \ln \Upsilon_i}{\sigma} \to \frac{\rho_{B-\bar{B}}\mu_{\rm B}}{T\sigma}\,. \tag{8}$$

Thus, in this limit at the RHIC energy range, we expect that $E_{\rm th}/TS \to 1/(1+P/\epsilon)$. However, the results in fig. 6 show that the chemical non-equilibrium effects contribute considerably.

It is interesting to note that the same behavior of the physical properties of the fireball has also been obtained as a function of the volume in the study of the impact parameter dependence, see fig. 4 in [3]. In fact, the results we derived show an unexpected universality of the hadronizing fireball, which depends solely on the question if it occurs "below" or "above" the threshold in energy

and volume size; the volume threshold corresponds to the critical participant number $13.4 < A^{\rm cr} < 25.7$.

At these values of A and the associated baryon content at central rapidity [3], the grand-canonical description of particle yields is still justified [80,81], also for strangeness. However, the fitted reaction volume (not further used in the present work) may be revised within the canonical approach by 10–20% for the most peripheral collisions studied in [3].

3.3 Strangeness and entropy yield

The yield of strangeness produced, should the deconfined QGP fireball be formed, is sensitive to the initial conditions, especially to the temperature achieved. The standard results for the strangeness relaxation time corresponds to $\tau_s(T = 300\,{\rm MeV}) \simeq 2\,{\rm fm}/c$ [82]. When this result is used in model calculations addressing RHIC [83], one finds, assuming gluon thermal and chemical equilibrium, that the thermal strangeness production in the early stage suffices to saturate the QGP fireball phase space at hadronization.

Even so, there is considerable uncertainty how short the time required to relax the strangeness flavor is, as the relaxation time lengthens with the square of the glue phase space under-occupancy, $\tau_s \propto 1/\gamma_{\rm G}^2$. Much of the uncertainty about the gluon chemical conditions prevailing in the initial thermal phase can be eliminated by considering the ratio of the number of strange quark pairs to the entropy s/S. In the QGP, the dominant entropy production occurs during the initial glue thermalization $\gamma_{\rm G} \to 1$, and the thermal strangeness production occurs in parallel and/or just a short time later. Moreover, both strangeness s and entropy S are nearly conserved in hadronization, and thus, the final-state yield value for the ratio s/S is directly related to the kinetic processes in the fireball at $\tau \simeq 1$–$3\,{\rm fm}/c$. A thorough discussion of the observable s/S is presented in [79], and detailed evaluation within a dynamical model of s/S was obtained [84]. The following is a motivating introduction to these developments.

We first estimate the magnitude of s/S in the QGP phase considering, in the hot early stage of the reaction, an equilibrated non-interacting QGP phase with perturbative properties:

$$\frac{s}{S} \equiv \frac{\rho_s}{\sigma} = \frac{\gamma_s^{\rm QGP}(3/\pi^2)T^3(m_s/T)^2K_2(m_s/T)}{(32\pi^2/45)T^3 + n_{\rm f}[(7\pi^2/15)T^3 + \mu_q^2T]}\,, \\ = \frac{0.03\gamma_s^{\rm QGP}}{1 + 0.054(\ln\lambda_q)^2}\,. \tag{9}$$

Here, we used for the number of flavors $n_{\rm f} = 2.5$ and $m_s/T = 1$. We see that the result is a slowly changing function of λ_q, for large $\lambda_q \simeq 4$ we find at lowest SPS energies, the value of s/S is reduced by 10%. Considering the slow dependence on $x = m_s/T \simeq 1$ of $W(x) = x^2K_2(x)$, there is further dependence on the temperature T.

The rise with reaction energy toward the limiting value, $s/S = 0.03$ for large $\sqrt{s_{\rm NN}}$, is driven by the decrease in $\lambda_q \to 1$ and, importantly, by an increase in the chemical strangeness equilibration with the QGP occupancy $\gamma_s^{\rm QGP} \to 1$. The dependence on the degree of chemical equilibration which dominates the functional behavior with $\sqrt{s_{\rm NN}}$ is

$$\frac{s}{S} = \frac{0.03\gamma_s^{\rm QGP}}{0.38\gamma_{\rm G} + 0.12\gamma_s^{\rm QGP} + 0.5\gamma_q^{\rm QGP} + 0.054\gamma_q^{\rm QGP}(\ln\lambda_q)^2}\,. \tag{10}$$

Equation (10) predicts a smooth increase in s/S toward its maximum value which by counting the degrees of freedom appears to be $s/S \to 0.03$, while the QGP source of particles approaches chemical equilibrium with increasing collision energy and/or increasing volume. It is important to keep in mind that the ratio s/S is established early on in the reaction, and the above relations and associated chemical conditions we considered apply to the early hot phase of the fireball. Yet, strangeness and entropy, once created, cannot disappear as the more complex low-temperature domain is developing. Specifically, near to hadron freeze-out, the perturbative QGP picture used above does not apply. Gluons are likely to freeze faster than quarks and both are subject to the much more complex non-perturbative behavior. But the value s/S is preserved across this non-perturbative domain.

In tables 8 and 9, we present, in the top portion, the strangeness production as a function of the reaction energy at AGS, SPS and RHIC, respectively. We give the baryon content and the total strangeness content of the fireball derived from the SHM fit to the particle yield. Below, we see the above-discussed strangeness per entropy s/S ratio, and strangeness per net baryon number s/b ratio. We present the increasing specific strangeness per baryon and per entropy yields in fig. 7, two top panels. The remarkable result we find is that the specific per entropy yield of strangeness converges for top RHIC energy and central rapidity toward the QGP result obtained counting the degrees of freedom, see eq. (9). The somewhat smaller values of s/b for the 4π case are consistent with the need to count all participant baryons.

The middle section, in tables 8 and 9, shows the center-of-momentum energy cost $\sqrt{s_{\rm NN}}/(2s/b)$ to make one strangeness pair. The micro-canonical input variables, s/V and b/V, for this entry vary significantly along with, and as a function of $\sqrt{s_{\rm NN}}$. Yet, we see that the result obtained varies smoothly, at first it diminishes finding a minimum at around $E = 40\,A$GeV and it rises slowly thereafter. It is clearly more energy expansive to make strangeness at AGS, nearly by a factor 2. A minimum in energy cost to make strangeness is near to 30 AGeV beam energy, at the peak of K^+/π^+ horn.

The increase in the cost of making strangeness can be attributed to the decreasing energy fraction stopped in the reaction. The energy stopping can be estimated by evaluating the per baryon thermal energy content $E_{\rm th}/b$ and obtaining from this the fraction of the initial energy converted into thermal energy in the final state, $(2E_{\rm th}/b)/\sqrt{s_{\rm NN}}$, whose fraction steadily drops from 75% at AGS to 48% at top SPS energy.

Table 8. AGS and CERN energy range (see top lines for the projectile energy E [GeV] and $\sqrt{s_{\rm NN}}$) the strangeness yield s ($=\bar{s}$), the strangeness per entropy s/S, the strangeness per baryon s/b, the energy cost to make strangeness pair $\sqrt{s_{\rm NN}}/(2s/b)$, the thermal energy per baryon at hadronization $E_{\rm th}/b$, the fraction of initial collision energy in thermal degrees of freedom $(2E_{\rm th}/b)/\sqrt{s_{\rm NN}}$.

E [AGeV]	11.6	20	30	40	80	158
$\sqrt{s_{\rm NN}}$ [GeV]	4.84	6.26	7.61	8.76	12.32	17.27
b	375.5	347.9	349.2	349.9	350.3	362.0
$\bar{s}$	35.5	70.3	100.8	110	161	218
$100\bar{s}/S$	0.788	1.26	1.94	1.90	2.16	2.22
$\bar{s}/b$	0.095	0.202	0.289	0.314	0.459	0.60
$\sqrt{s_{\rm NN}}/(2\bar{s}/b)$ [GeV]	25.5	15.5	13.1	13.9	13.4	14.4
$E_{\rm th}/b$ [GeV]	1.82	2.26	2.33	2.58	3.30	4.08
$(2E_{\rm th}/b)/\sqrt{s_{\rm NN}}$	0.752	0.722	0.612	0.589	0.536	0.472
$E_{\rm th}/\bar{s}$ [GeV]	19.25	10.9	8.08	8.21	7.19	6.80

Table 9. Top section: SHM yields of baryon b and at central rapidity $\mathrm{d}b/\mathrm{d}y$, and strangeness s and $\mathrm{d}s/\mathrm{d}y$ at RHIC, left for the total system, right for the central rapidity region. Next, we give the strangeness per entropy s/S (for central rapidity: $\mathrm{d}s/\mathrm{d}S$), the strangeness per baryon s/b, the energy cost to make the strangeness pair $\sqrt{s_{\rm NN}}/(2\mathrm{d}s/\mathrm{d}b)$, the thermal energy per baryon at hadronization $\mathrm{d}E_{\rm th}/\mathrm{d}b$, the fraction of initial collision energy in thermal degrees of freedom, $(2E_{\rm th}/b)/\sqrt{s_{\rm NN}}$. All 62.4 GeV results, and the 130 GeV 4π results, are result of assumptions, and/or interpolation of yields, and/or parameters, and hence are a prediction.

$\sqrt{s_{\rm NN}}$ [GeV]	62.4	130	200	62.4	130	200
	$N_{4\pi}$			$\mathrm{d}N/\mathrm{d}y\|_{y=0}$		
b, $\mathrm{d}b/\mathrm{d}y$	350	350	350	33.5	18.5	14.8
$\bar{s}$, $\mathrm{d}\bar{s}/\mathrm{d}y$	560	755	726	120.4	136.7	123
$100\bar{s}/S$, $\mathrm{d}\bar{s}/\mathrm{d}S$	3.17	2.43	2.66	3.30	3.39	3.13
$\bar{s}/b$, $\mathrm{d}\bar{s}/\mathrm{d}b$	1.60	2.16	2.07	3.35	6.87	8.29
$\sqrt{s_{\rm NN}}/(2\mathrm{d}\bar{s}/\mathrm{d}b)$ [GeV]	19.5	30.1	48.3	9.31	9.46	12.06
$\mathrm{d}E_{\rm th}/\mathrm{d}b$ [GeV]	7.18	9.52	11.24	14.8	30.4	38.2
$(2\mathrm{d}E_{\rm th}/\mathrm{d}b)/\sqrt{s_{\rm NN}}$	0.230	0.146	0.112	0.474	0.467	0.382
$\mathrm{d}E_{\rm th}/\mathrm{d}\bar{s}$ [GeV]	4.49	4.41	5.41	4.42	4.42	4.60

In terms of thermal energy, the cost of making strangeness pair is given in the last line of tables 8 and 9. After an initial very rapid drop from the AGS cost at 20 GeV to 8 GeV near to the top of the horn, there follows a very slow and gradual decrease. We show this result graphically in the bottom panel in fig. 7. This behavior clearly shows a *rapid* but smooth change-over in the underlying mechanism of strangeness production with increasing reaction energy, between 11.6 and 30 AGeV. Once the new mechanism is fully operational, we have essentially a flat, slowly decreasing energy cost per strangeness. The drop we observe above 30 AGeV can be thought to originate in the transfer of thermal energy to the kinetic energy of collective expansion which we do not record in our analysis, and thus, it is conceivable that the cost in actual energy remains constant above $\sqrt{s^{\rm cr}_{\rm NN}}$.

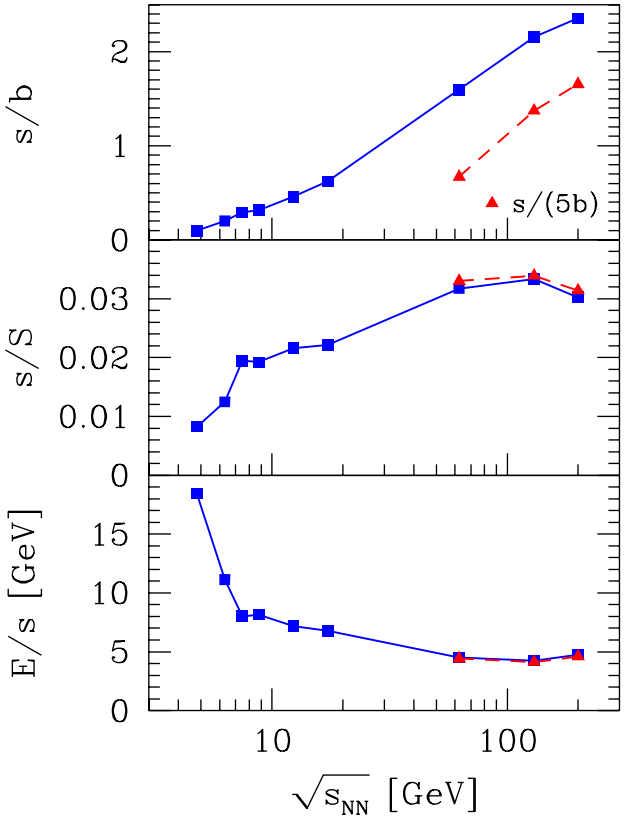

Fig. 7. (Colour on-line) The specific strangeness yield as a function of the reaction energy $\sqrt{s_{\rm NN}}$. Top: strangeness per baryon $\bar{s}/b$; center: strangeness per entropy $\bar{s}/S$ and bottom: $E_{\rm th}/\bar{s}$ thermal energy content per strangeness. Solid squares correspond to $N_{4\pi}$ the triangles on the right are for the rapidity density yield $\mathrm{d}N/\mathrm{d}y$ at RHIC. The total yield results are connected by a solid line to guide the eye, and the central rapidity results (red) are connected by a dashed line.

As the bottom right of table 9 indicates, the fraction of energy stopped in the central rapidity region at RHIC, $(2\mathrm{d}E_{\rm th}/\mathrm{d}b)/\sqrt{s_{\rm NN}}$ is rather large, it is estimated to be 47% at $\sqrt{s_{\rm NN}}=62.4$ GeV decreasing to 38% at top RHIC energy. The energy cost to make strangeness extrapolates well from the SPS level, connecting smoothly, see the bottom panel in fig. 7, for both total yield and central rapidity yield. We note, in passing, that only a small fraction, 10%, of the total energy is thermalized at the top RHIC energy considering the total fireball. 90% is evidently the energy of the collective flow, predominantly in the longitudinal direction.

The expectation of ever rising strangeness yield with $\sqrt{s_{\rm NN}}$ is not disappointed in fig. 8, but the rapid smooth rise is surprising. One finds such a result in a nearly model-independent analysis adding up the $\bar{s}$ carrier particles, which are mostly directly measured. A more precise study which adds up strangeness in the particles produced according to the SHM as seen in tables 8 and 9 is shown in fig. 8 —there are non-negligible contributions of unobserved hidden strangeness, in particular in the η hadron (40% $s\bar{s}$ content). We have scaled the strangeness yield to

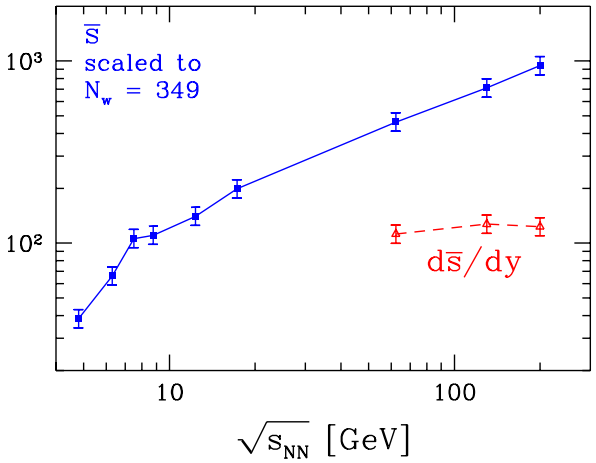

Fig. 8. (Colour on-line) The strangeness $\bar{s}$ (= s) content resulting from the SHM fit, as a function of the reaction energy. The total yield results, solid squares (blue), are scaled with number of wounded nucleons to a fireball formed in 7% central Pb–Pb reactions ($N_{\rm W} = 349$). The triangles, on the right, are for the rapidity density yield $\mathrm{d}\bar{s}/\mathrm{d}y$ at RHIC.

the 7% centrality with $N_{\rm W} = 349$ for the total yields. For the central rapidity, we present results for the 5% centrality.

4 Discussion and interpretation

4.1 The K^+/π^+ horn

One can wonder how, in qualitative terms, can a parameter γ_q, which controls the light quark yield, help explain the horn structure seen in fig. 2. We observe that this horn structure in the K^+/π^+ ratio traces the final-state valence quark ratio $\bar{s}/\bar{d}$, and in the language of quark phase space occupancies γ_i and fugacities λ_i, we have:

$$\frac{K^+}{\pi^+} \to \frac{\bar{s}}{\bar{d}} \propto F(T) \left(\frac{\lambda_s}{\lambda_d}\right)^{-1} \frac{\gamma_s}{\gamma_d} \simeq F(T) \left(\lambda_{I3}\frac{\lambda_s}{\lambda_q}\right)^{-1} \frac{\gamma_s}{\gamma_q}\,. \tag{11}$$

In chemical equilibrium models $\gamma_s/\gamma_q = 1$, and the horn effect must arise solely from the variation in the ratio λ_s/λ_q and the change in the temperature T. The isospin factor λ_{I3} is insignificant in this consideration. For the interesting range of freeze-out temperature, $F(T)$ is a smooth function of T. Normally, one expects that T increases with the collision energy, hence we expect a monotonic increase in the K^+/π^+ ratio, not considering the quark chemistry.

As the collision energy is increased, the increased hadron yield leads to a decreasing $\lambda_q = e^{\mu_{\rm B}/3T}$. We recall the smooth decrease of $\mu_{\rm B}$ with the reaction energy seen in the bottom panel in fig. 5. The two chemical fugacities λ_s and λ_q are coupled by the condition that the strangeness is conserved. The chemical potential effect is suggesting a smooth increase in the K^+/π^+ ratio. With considerable effort, one can arrange the chemical equilibrium fits to bend over at $\sqrt{s^{\rm cr}_{\rm NN}}$ as the dotted line in fig. 2 shows. It is quasi-impossible to generate a sharp horn with the chemical equilibrium model.

The consideration of chemical non-equilibrium allows us to consider an energy-dependent ratio γ_s/γ_q, which, as seen in eq. (11), is a multiplicative factor in the horn structure. The fit produces a horn-like behavior of γ_s/γ_q at $\sqrt{s^{\rm cr}_{\rm NN}}$, seen in fig. 5. As a function of energy, many other particle yields must remain relatively smooth, with a few exceptions seen in fig. 3. We see that the description of the horn structure is possible, as there are effectively three functions of $\sqrt{s_{\rm NN}}$ which help to create it, T, λ_q/λ_s and γ_s/γ_q, but it is in no way assured that the right horn arises, seen the behavior with the energy of the other particle yields.

Indeed, only the full chemical non-equilibrium model in which the two phase space occupancies, γ_s and γ_q, vary independently, does a good job, as is seen comparing the solid with dashed and dotted lines in fig. 2. Seen the horn-like structure of all these lines obtained relaxing strangeness conservation constraint we realize that it is not the increased number of parameters, but the fact that particle production follows the SHM with chemical non-equilibrium which allows the non-equilibrium model to succeed.

4.2 The K^+/π^+ horn as a function of the reaction volume

The rather sudden changes in the freeze-out parameters γ_q and T appears to be a universal behavior. We established it here as a function of energy, and in earlier work as a function of the reaction volume (*i.e.*, participant number A), see fig. 1 in [3]. In both cases, the chemical freeze-out temperature is higher below a threshold, as expressed either by low energy or participant number. The most drastic change is that γ_q jumps up from a value at, or below 0.5, to 1.6 as either the energy or volume threshold is crossed. The volume threshold is, however, not as sharp as the reaction energy threshold. The large system limit is achieved for $A > 25$, with a smooth transition beginning at $A > 6$, as can be seen in fig. 4 in [3].

Seeing this remark, one immediately wonders if the K^+/π^+ horn is present in the impact parameter kaon and pion data and the answer is no. Actually, this is not surprising: since both π^+ and K^+ originate, in our study, at the level of about 50% in directly thermally produced particles the ratio K^+/π^+ is a measure of the horn structure due to a rise in density of strangeness $\bar{s}$ at hadronization, outpaced by the rise in the $\bar{d}$ density above $\sqrt{s^{\rm cr}_{\rm NN}}$, whatever the mechanism in terms of statistical parameters that implements this. However, when considering the impact parameter dependence at $\sqrt{s_{\rm NN}} = 200\,\mathrm{GeV}$, the rise in strangeness has yet to occur, as in the small volume there has insufficient life span to produce strangeness. In this situation we do not expect that the horn is present as a function of A.

One can see the delayed production of strangeness as a function of the impact parameter directly in the PHENIX impact parameter data [62], without need for a detailed

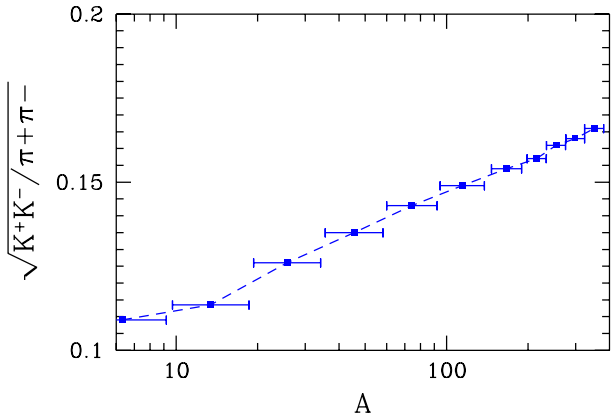

Fig. 9. $\sqrt{K^+K^-/\pi^+\pi^-}$ as a function of the participant number A varying with reaction centrality, PHENIX data [62].

theoretical analysis. Consider the ratio shown in fig. 9: $K/\pi \equiv \sqrt{K^+K^-/\pi^+\pi^-}$. This particular product ratio of particles is nearly independent of the chemical potentials $\mu_{\rm B}$, $\mu_{\rm S}$ and the volume V, since it comprises ratio of products of particles and antiparticles. The rise seen in fig. 9 is evidence for an additional strangeness production mechanism turning on at about $A \simeq 20$. In fig. 9 we do not show a common systematic error, thus the normalization scale of the figure could undergo a revision. This cannot change the insight that the additional strangeness above and beyond the first collision content is produced for $A > 20$, enhancing the global yield by 50% or more. Moreover, we see that the rise is gradual as can be expected in kinetic theory models of strangeness production [82,84], and there is at the maximum centrality no evidence as yet of strangeness yield saturation.

The entropy content of the small system $A < 20$ is such that the strangeness per entropy is at the level of $s/S \simeq 0.02$, and both entropy and strangeness rise with the centrality of the reaction at $\sqrt{s_{\rm NN}} = 200\,{\rm GeV}$. However, unlike the energy dependence, the ratio s/S rises modestly, strangeness does not outpace the entropy rise by more than 20%. This is in agreement with expectation, since the threshold of the strangeness mass is not fully relevant at the top RHIC reaction energy, and thus we are seeing the properties of a deconfined initial state in which the strange quark is effectively massless. Instead, it is the lifespan of the system that matters, as noted above.

There is a very little observed dependence of ratios of hadron resonances with the ground-state yields, such as K^*/K. This implies and agrees in quantitative way with the tacit assumption inherent in the above discussion, and the result of a more detailed analysis [3], that there is no T-dependence of the freeze-out conditions for $A > 20$. For this reason, for $A > 20$ ratios of all hadrons which do not involve a difference in the strangeness content do not vary with centrality.

We further note that there is little change in chemical potentials with centrality for $A > 20$, indicating that the stopping of baryons is not a result of multiple scattering, but is due to phase conditions of matter. Comparing other properties of matter, we see very much the same behavior as a function of the impact parameter and reaction energy: in particular, we note the step up in pressure, in energy density, and in entropy density at the impact parameter threshold [3].

4.3 Chemical equilibrium or non-equilibrium?

An important question discussed in the study of hadron yields interpretations is if chemical equilibrium or non-equilibrium prevails in the hadronization process. There are workers who strongly defend the chemical equilibrium SHM [85]. Let us look again at the survey of the fit quality results seen in fig. 1. We note that for $\gamma_q = 1$ (but $\gamma_s \neq 1$) at each energy there seems to exist a reasonable fit with $0.5 < \chi^2/{\rm d.o.f.} < 1.5$ for the data sample considered, which suggests that at each reaction energy with $\gamma_q = 1$ a reasonable and widely accepted physical description of the experimental data emerges. This result is therefore claimed in studies that focus on the hadron yields at each energy separately. What works poorly in SHM used with $\gamma_q = 1$ and even worse with $\gamma_q = 1$, $\gamma_s = 1$ is the energy dependence of particle ratios, with the most prominent present-day example being the horn structure in the K^+/π^+ yield ratio. Seen from this perspective, it is the energy-dependent particle yield that requires the inclusion in the necessary set of parameters of a varying value $\gamma_q \neq 1$.

Another important question directly related to the issue of chemical equilibrium and non-equilibrium is how the fitted results for $T(\mu_{\rm B})$, the "hadronization curve" relate to the phase boundary between the deconfined primary phase and the hadron phase. Clearly, the results of the fit are greatly dependent on the assumption about the chemical condition with the equilibrium fit claiming a hadronization at RHIC at $T = 175\,{\rm MeV}$.

The rapidly decreasing freeze-out temperature T as $\sqrt{s_{\rm NN}}$ decreases, and which is certainly inconsistent with the rather flat phase transition boundary at moderate chemical potentials is explained by suggesting that the hadronization may be related to a particular value of energy per particle content, of magnitude 1 GeV [85]. However, this condition, though not rooted in any known basic physical principle, is also obtained in some dynamical studies, see, *e.g.*, refs. [86,87]. We note that the chemical equilibrium hypothesis fails to explain the hadronization conditions expected as a function of T and $\mu_{\rm B}$, or equivalently, as a function of $\sqrt{s_{\rm NN}}$.

In summary, the interpretation of hadron production in terms of chemical equilibrium SHM disagrees, in quantitative manner, both with the reaction energy-dependent particle yields (such as the K^+/π^+ horn) and the reaction energy-dependent shape of hadronization boundary.

4.4 Hadronization boundary in heavy-ion collisions

We believe that the hadronization boundary, in the T-$\mu_{\rm B}$ plane, is the result of a complex interplay between the dynamics of the heavy-ion reaction and the properties of

both phases of matter, the inside of the fireball, and the hadron phase we observe. Even disregarding complications related to the rapid expansion of the dense matter fireball, the presence of chemical non-equilibrium particle distributions introduces significant freedom into the shape and location of the $T(\mu_{\rm B})$ transition region.

Recall, first, that available lattice results apply to a system in the thermodynamic limit with $\gamma_q = \gamma_s = 1$, for both quark and confined hadron phases. The typical boundary between the QGP and hadron phases is discussed in ref. [77], and is dependent on the chemical properties of QGP. Typically, one considers the dependence on chemical potentials, and in particular on $\mu_{\rm B}$, however, a significant change in the phase boundary location is to be expected when γ_q and $\gamma_s \neq 1$. To understand this important remark, consider the two other known cases $\gamma_q = 1$, $\gamma_s = 0$ corresponding to 2 flavors, and $\gamma_q = \gamma_s = 0$ corresponding to pure gauge. There is a significant change in $T(\mu_{\rm B} = 0)$, which increases with decreasing γ_i.

Moreover, not only the location but also the *nature* of the phase boundary can be modified by the variation of γ_i. We recall that for the $2 + 1$ flavor case, there is possibly a critical point at the finite baryochemical potential with $\mu_{\rm B} \simeq 350\,{\rm MeV}$ [77,88]. However, for the case of 3 massless flavors there can be a 1st-order transition at all $\mu_{\rm B}$ [89,90]. Considering a classical particle system, one easily sees that an over-saturated phase space, *e.g.*, with $\gamma_q = 1.6$, $\gamma_s \geq \gamma_q$ for the purpose of the study of the phase transition acts as being equivalent to a system with 3.2 light quarks and 1.6 massive (strange) quarks present in the confined hadron phase.

Even though one should be keenly aware that oversaturation of the phase space is not the same as additional degeneracy due to true degrees of freedom, the similarity of the resulting effect must be considerable. We know that with increasing $\mu_{\rm B}$, the increased quark density creates the environment in which the phase cross-over becomes a phase transition. The influence of $\gamma_{q,s}^{\rm QGP}$ cannot be different. Considering that $\gamma_{q,s}^{\rm QGP}$ enhances both the quark and antiquark number, it should be more effective compared to $\mu_{\rm B}$ in its facilitation of a phase transition, and in the reduction of the temperature of the phase boundary for $\gamma_{q,s}^{\rm QGP} > 1$.

We therefore can expect that, for a chemically oversaturated system, there is also an effective increase in the number of degrees of freedom. Looking at the structure of the quark-hadron transformation this increase in the number of available effective degrees of freedom occurs in a physical system which is almost, but not quite, able to undergo a 1st-order phase transition. Considering here also the sudden nature of the fireball breakup seen in several observables [1], we conjecture that the hadronizing fireball leading to $\gamma_s > \gamma_q = 1.6$ passes a true phase boundary corresponding to a 1st-order phase transition condition at small $\mu_{\rm B}$. Because of the changed count in the degrees of freedom, we expect that the phase transition temperature is at the same time decreased to below the cross-over value for the chemical equilibrium case of $2 + 1$ flavors near $T = 162 \pm 3\,{\rm MeV}$.

It seems to us that it would be very interesting to determine, in a rigorous way for the case of the $2 + 1$ flavor lattice QCD at $\mu_{\rm B} = 0$ for which values, if any, of γ_i the system undergoes a phase transition of 1st order. Lattice QCD methods employed to obtain results at finite $\mu_{\rm B}$, *e.g.*, the power expansion [88,91], should also allow to study the case of $\mu_\gamma \equiv T \ln \gamma_i > 0$, and near to $\mu_\gamma =$, *i.e.* $\gamma_i = 1$. We see the actual difficulty in the need to simulate different values of μ_γ in the two phases, such that the quark pair content is preserved across the phase boundary.

The dynamical, and theoretically less spectacular, effect capable to shift the location in temperature of the expected phase boundary, is due to the expansion dynamics of the fireball. The analysis of the RHIC results suggests that the collective flow occurs at parton level [92]. Collective flow of color (partons) is like a wind capable to push out the color non-transparent "true" vacuum [93], adding to thermal pressure the dynamical component, for a finite expanding system this would lead to supercooling [94]. This dynamical effect will push the hadronization condition to lower local freeze-out T at high $\sqrt{s_{\rm NN}}$, thus flattening the boundary between the phases as a function of $\mu_{\rm B}$. In the context of the results we have obtained, it is the smoothness of the ratio P/ϵ obtained at hadronization which supports the possible relevance of the dynamic phase boundary displacement. This behavior suggests a smoothly changing dynamical break-up condition, potentially related to (hydrodynamic) flow.

4.5 Our hadronization boundary and its interpretation

The above two effects, the change in the location of the static phase boundary in the presence of chemical *non*-equilibrium and the dynamics of collective matter flow toward the breakup condition, are both non-negligible but hard to evaluate quantitatively. We believe that they can explain why the chemical freeze-out conditions T and $\mu_{\rm B}$ are as presented in fig. 5. Of particular relevance is the low value of T at high reaction energy, and relatively high value of T at low reaction energy, just opposite to what one finds to be the result of the SHM analysis when chemical equilibrium is assumed.

Our chemical freeze-out conditions are better shown in the T-$\mu_{\rm B}$ plane, see fig. 10. Considering the results shown in fig. 5, we are able to assign to each point in the T-$\mu_{\rm B}$ plane the associate value of $\sqrt{s_{\rm NN}}$. The RHIC ${\rm d}N/{\rm d}y$ results are to the outer left. They are followed by RHIC and SPS $N_{4\pi}$ results. The dip corresponds to the 30 and 40 AGeV SPS results. The top right is the lowest 20 AGeV SPS and top 11.6 AGeV AGS energy range. We see that the chemical freeze-out temperature T rises for the two lowest reaction energies 11.6 and 20 AGeV to near the Hagedorn temperature, $T = 160\,{\rm MeV}$. Such phase structure is discussed, *e.g.*, in the context of chiral quark pairing [12].

The size of the error bars, in fig. 10, is the output of the fit process, and when it is rather large, it implies that the resulting χ^2 profile was relatively flat, or/and that

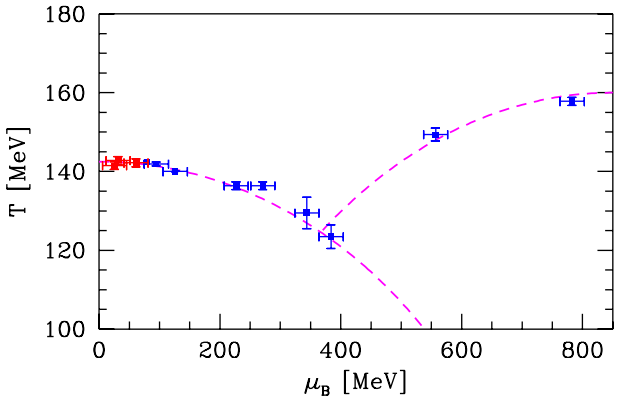

Fig. 10. T-μ_B plane with points obtained in the SHM fit. See text for discussion.

there were two neighboring good fit minima. To guide the eye, we have added two lines connecting the fit results. As seen in fig. 10, at $\mu_B = 0$, we find that hadronization occurs at $T = 140$, decreasing to $T = 120\,\mathrm{MeV}$ at $\mu_B = 400\,\mathrm{MeV}$. Along this line $\gamma_q > 1.6$. As argued in the previous sect. 4.4, this line could be a true 1st-order phase boundary between quark matter and an over-saturated hadron phase.

Two different interpretations come to mind when we attempt to understand the other branch in fig. 10, the rise from $T \simeq 120$ to 160 for $\mu_B > 400$, which is accompanied by a rather low hadron side phase space occupancy. Most "natural" is to presume that the dissolution of color bonds did not occur in heavy-ion collisions below 30 AGeV, we are dealing with "conventional" hadron matter. The under-saturation occurs since there was no time to make hadrons, *i.e.*, chemical equilibration was not achieved in the colliding hadron system before it breaks apart.

The fireball break-up at a higher temperature is a consistent freeze-out scenario for under-saturated hadron phase space considering the kinetic scattering freeze-out condition. Given the greatly reduced particle density ($\propto \gamma_q^n$, $n = 3, 2, 1$) a high T freeze-out for $\gamma_i < 0.5$ is consistent. The nucleon density scales with γ_q^3 and pion density with γ_q^2. Therefore the meson-baryon and meson-meson scattering lengths, which scale as $L \propto 1/\gamma^5$, and $L \propto 1/\gamma^4$, respectively, given the small L. This implies that, as the system expands, it is able to freeze out early at a higher T.

On the other hand, the volume size we found, see table 1, is significantly larger at low reaction energies. This implies that a scenario with pure hadron matter present is subject to a quite different expansion history. This signals that a standard picture of a conventional hadron matter formation at reaction energies below the transition point at $6.26\,\mathrm{GeV} < \sqrt{s_{\mathrm{NN}}^{\mathrm{cr}}} < 7.61\,\mathrm{GeV}$ may not be the valid explanation of the results of our analysis. Namely, if the reaction history since the first contact is different for the two reaction energy ranges, one would expect that the systematics of the final-state entropy production, strangeness production, and strange antibaryon production has a visible break at the critical point. What we have found is, instead, that these quantities show a rather smooth uninterrupted rise with the reaction energy.

This means that the initial conditions reached in the reaction where, *e.g.*, entropy and strangeness are produced, is not undergoing a sudden change. The change occurs at the end near to the hadronization of matter. For this reason, we see a change in particle yields (the horn), statistical parameters jump, and the physical conditions at hadronization jump even more. The yields of quantities which are driven by the physics of the initial dense matter formation, *e.g.*, the entropy content, strangeness content, change smoothly with the heavy-ion reaction energy in the domain we explored. We are, furthermore, swayed away from the picture of the hadronic gas being the form of matter at break-up below $\sqrt{s_{\mathrm{NN}}^{\mathrm{cr}}}$ by the strange antibaryon production systematics we discussed in fig. 4.

We are searching thus for an explanation in terms of a new phase of matter being involved in the hadronization process, but clearly this cannot be the semi-perturbative quark-gluon plasma state. The conceivable explanation of the fit result below 30 AGeV is the presence, at the high baryon density arising at large μ_B, of a constituent quark plasma [95]. Even if the perturbative QCD quark phase is reached at high temperature, in expansion cooling the system encounters the valon (word derived from "valence" quark) phase in which the color quark bonds are broken, but the chiral symmetry restoration is not completed, with quarks of mass $m_{u,d} \simeq 340\,\mathrm{MeV}$ and $m_s \simeq 500\,\mathrm{MeV}$ being the only active degrees of freedom. This scenario is not inconsistent with the finding on the lattice, that, for $\mu_B \to 0$ and in chemical equilibrium, the chiral symmetry restoration coincides with the deconfinement transition.

In a valon matter, even assuming chemical equilibrium, the number of quark pairs at temperature near to $T = 160\,\mathrm{MeV}$ would be rather small, given the high constituent quark mass. In the break-up of this system, a relatively small γ_i^{HG} is achieved. Furthermore, since the mass of these constituent quarks is greater than that of the pion, the phase transformation between hadron and valon matter occurs at relatively large T. To see this, recall that the pion with its low mass produces greater pressure than valons and thus is pushing the transition boundary to higher T. Strangeness, and importantly the entropy content in this phase arise due to prior initial state perturbative QGP phase and hence such a valon system must be larger in volume at the point of hadronization.

It is also conceivable that a hadron fireball evolving from the beginning and fully in the valon phase would maintain much of the continuity we saw in hadronic observables. For example, u and d valon-quark scattering can produce strange valon-quark pairs, and these give rise in hadronization to the abundances of strange antibaryons, as expected in the deconfined phase. What speaks for this option is the rather sudden change in the thermal energy content per strange quark pair produced, which is seen at the bottom of fig. 7, indicating the appearance of a new energy efficient mechanism of strangeness production above $\sqrt{s_{\mathrm{NN}}^{\mathrm{cr}}}$.

One may wonder how our findings compare to earlier studies of the phase boundary, both in statistical models [96], and microscopic models (see ref. [87] and references therein). In the microscopic models one accomplishes a better understanding of the approach to thermal and chemical equilibrium of the degrees of freedom employed. A continuous phase boundary is, here, a direct outcome of the assumption made about the degrees of freedom present. Our analysis, which does not rely on such assumptions, is thus less model dependent and allows for the presence of degrees of freedom with unexpected properties. On the other hand, we also firmly believe, as is shown in fig. 10 that there is a smooth phase boundary, with T dropping with increasing $\mu_{\rm B}$. What our study has uncovered is the possible presence of another phase boundary for $\mu_{\rm B} > 350\,{\rm MeV}$ at higher T. It is important for the reader to keep in mind that this finding is not in conflict with theoretical chemical equilibrium results which focus on the other, conventional, phase branch and address the physics of phase transformation occurring in the early Universe.

Moreover, a recent study of the low-energy AGS pion production data [97] found that the thermal freeze-out temperature at a reaction energy of 8 GeV is at $T_{\rm th} = 140\,{\rm MeV}$ [98]. Thus, there is also consistency of our present analysis with the shape of pion transverse mass spectra and the high chemical freeze-out temperature we find at AGS. Another interesting finding was the medium mass modification which allowed to describe pion decay spectra.

4.6 Final remarks

In summary, we have performed a complete analysis of the energy dependence of hadron production in heavy-ion collisions, spanning the range beginning at the top AGS energy, to the top RHIC energy. We have made extensive predictions about particle production in the entire energy range. These results are useful in several respects. For example, we have shown that the best energy to search for the elusive pentaquarks would be at SPS at 30–40 AGeV, where we find that the total yield of $\Theta^+(1540)$ is already fully developed. Thus, there is a maximum in the ratio $\Theta^+/K_{\rm S} \simeq 0.2$ at 30 AGeV. Of course, this finding presupposes the existence of the exotic state.

We have furthermore presented hadron yields important in the understanding of dilepton spectra, such as ρ, η and ω. The relative meson resonance yields we find do not follow the pp systematics and vary as a function of energy. Thus one can test the hadronization picture here presented in the study of resonance production. This observation was recently exploited in a systematic fashion [99].

We have shown that the threshold in energy which generates a horn in the K^+/π^+ yield ratio can be associated with the chemical freeze-out shifting rather rapidly toward a condition of greatly increased hadronization densities. This transition separates the high entropy density phase at a high heavy-ion reaction energy from a low entropy density phase. This behavior parallels the findings for the impact parameter dependence of RHIC results, where the low entropy density phase is seen for small reaction volumes present at large impact parameters [3].

Several observables, including strangeness production, show continuity across the energy threshold at $6.26\,{\rm GeV} < \sqrt{s_{\rm NN}^{\rm cr}} < 7.61\,{\rm GeV}$, thus, it seems that the critical conditions expresses a change in the nature of the fireball breakup, and to a lesser degree a reaction-energy-dependent change in the nature of initial conditions reached in the reaction.

We have discussed, in depth, our findings about the hadronization condition $T(\mu_{\rm B})$ and have argued that at high reaction energies a 1st-order phase transition is arising in the chemically non-equilibrated hot hadronic matter system. A detailed discussion was presented about possible changes in the phases of hadronic matter as a function of the reaction energy and reaction volume.

The manuscript nucl-th/0504028, on which this work is based, has been first web-published in April, 2005. We undertook the current revision to correct an entropy yield error which the early SHARE release contained. This changes the entropy S related table entries and figures, the data fits are unaffected. When redoing the fits to obtain entropy, we incorporated the latest strange hadron yields of NA49 as available. We thank NA49 and PHENIX Collaborations for valuable comments regarding the acceptances of weak decays. We thank M. Gaździcki and G. Torrieri for valuable comments. The work is supported in part by a grant from the U.S. Department of Energy DE-FG02-04ER4131. LPTHE, Université Paris 6 et 7 is Unité mixte de Recherche du CNRS, UMR7589.

References

1. For theoretical evaluation, see Nucl. Phys. A **750**, Issue 1, pp. 1-171 (March 2005); for experimental evaluation, see Nucl. Phys. A **757**, Issue 1, pp. 1-283 (August 2005).
2. NA49 Collaboration (M. Gaździcki *et al.*), J. Phys. G **30**, S701 (2004).
3. J. Rafelski, J. Letessier, G. Torrieri, Phys. Rev. C **72**, 024905 (2005) arXiv:nucl-th/0412072.
4. J. Letessier, J. Rafelski, Phys. Rev. C **59**, 947 (1999).
5. J. Kapusta, B. Muller, J. Rafelski, *Quark-gluon plasma: Theoretical foundations, an annotated reprint collection*, (Elsevier, Amsterdam, 2003) and references therein.
6. J. Rafelski, B. Müller, Phys. Rev. Lett. **48**, 1066 (1982); **56**, 2334 (1986)(E).
7. N.K. Glendenning, J. Rafelski, Phys. Rev. C **31**, 823 (1985); note that in fig. 2 the pion yield from resonance decays is not included, this dilutes the expected yields by about a factor two, flattening the curve.
8. J. Letessier, A. Tounsi, U. Heinz, J. Sollfrank, J. Rafelski, Phys. Rev. Lett. **70**, 3530 (1993); Phys. Rev. D **51**, 3408 (1995).
9. P. Koch, B. Muller, J. Rafelski, Phys. Rep. **142**, 167 (1986).
10. P. Koch, J. Rafelski, Nucl. Phys. A **444**, 678 (1985).
11. J. Rafelski, M. Danos, *Perspectives In High-Energy Nuclear Collisions*, NBSIR-83-2725 and GSI-83-6, see sect. 5, KEK scan available at `http://ccdb3fs.kek.jp/cgi-bin/img_index?200031578`; update: Lect. Notes Phys.

231, 361 (1985); M. Danos, J. Rafelski, Heavy Ion Phys. **14**, 97 (2001) (M. Danos memorial volume).
12. M. Kitazawa, T. Koide, T. Kunihiro, Y. Nemoto, Phys. Rev. D **65**, 091504(R) (2002).
13. M. Gaździcki, Acta Phys. Pol. B **34**, 5771 (2003); M. Gaździcki, M.I. Gorenstein, Acta Phys. Pol. B **30**, 2705 (1999).
14. G. Torrieri, W. Broniowski, W. Florkowski, J. Letessier, J. Rafelski, Comput. Phys. Commun. **167**, 229 (2005) and references therein; G. Torrieri, S. Jeon, J. Letessier, J. Rafelski, Comput. Phys. Commun. **175**, 635 (2006), and see further updates at `www.physics.arizona.edu/~torrieri/SHARE/share.html`.
15. G. Torrieri, J. Rafelski, J. Phys. G **30**, S557 (2004).
16. J. Letessier, J. Rafelski, Int. J. Mod. Phys. E **9**, 107 (2000).
17. P. Koch, J. Rafelski, W. Greiner, Phys. Lett. B **123**, 151 (1983).
18. BRAHMS Collaboration (I.G. Bearden *et al.*), Phys. Rev. Lett. **90**, 102301 (2003).
19. F. Becattini, J. Cleymans, A. Keranen, E. Suhonen, K. Redlich, Phys. Rev. C **64**, 024901 (2001).
20. NA49 Collaboration (V. Friese), Nucl. Phys. A **698**, 487 (2002).
21. J. Rafelski, J. Letessier, G. Torrieri, Phys. Rev. C **64**, 054907 (2001); **65**, 069902 (2002)(E).
22. J.I. Kapusta, S.M.H. Wong, Phys. Rev. Lett. **86**, 4251 (2001).
23. J. Letessier, J. Rafelski, G. Torrieri, *Deconfinement energy threshold: Analysis of hadron yields at 11.6-A-GeV*, arXiv:nucl-th/0411047.
24. The results of the NA49 experiment used here have been proved upon our request by M. Gazdzicki and B. Lungwitz (private communication, compilation of September 2006), whose documentation includes the explanation of the treatment of weak decays. Among the sources of these results, we note, in particular, the follwoing works [2,20,25–51]. The abstraction of these 28 works with in part not entirely consistent result tables (due to varying WD corrections, and some time dependence of preliminary results) into a 11 page table set appears to us to be solely possible by these key members of the NA49 Collaboration. We thank Drs. M. Gazdzicki and B. Lungwitz, for their kind help.
25. NA49 Collaboration (C. Blume), J. Phys. G **31**, S685 (2005).
26. The NA49 Collaboration (V. Friese *et al.*), J. Phys. G **30**, S119 (2004).
27. C. Alt *et al.*, Phys. Rev. C **73**, 044910 (2006).
28. NA49 Collaboration (A. Richard), J. Phys. G **31**, S155 (2005).
29. NA49 Collaboration (C. Blume), J. Phys. G **31**, S685 (2005).
30. The NA49 Collaboration (C. Alt *et al.*), J. Phys. G **30**, S119 (2004).
31. NA49 Collaboration (P. Dinkelaker), J. Phys. G **31**, S1131 (2005).
32. The NA49 Collaboration (S.V. Afanasiev *et al.*), Phys. Rev. C **66**, 054902 (2002).
33. T. Anticic *et al.*, Phys. Rev. C **69**, 024902 (2004).
34. S.V. Afanasiev *et al.*, Nucl. Phys. A **715**, 161 (2003).
35. NA49 Collaboration (T. Anticic *et al.*), Phys. Rev. Lett. **93**, 022302 (2004).
36. NA49 Collaboration (C. Meurer), J. Phys. G **30**, S1325 (2004).
37. NA49 Collaboration (M. Mitrovski), Acta Phys. Hung. A **24**, 157 (2005).
38. NA49 Collaboration (C. Alt *et al.*), Phys. Rev. Lett. **94**, 192301 (2005).
39. NA49 Collaboration (J. Bachler *et al.*), Nucl. Phys. A **661**, 45 (1999).
40. NA49 Collaboration (C. Alt *et al.*), Eur. Phys. J. C **45**, 343 (2006).
41. NA49 Collaboration (S.V. Afanasev *et al.*), J. Phys. G **27**, 367 (2001).
42. NA49 Collaboration (S.V. Afanasev *et al.*), Phys. Lett. B **491**, 59 (2000).
43. NA49 Collaboration (C. Alt *et al.*), *Pion and kaon production in central* Pb + Pb *collisions at 20A and 30A* GeV*: Evidence for the onset of deconfinement*, arXiv:0710.0118 [nucl-ex].
44. NA49 Collaboration (T. Susa), Nucl. Phys. A **698**, 491 (2002).
45. NA49 Collaboration (C. Alt *et al.*), Phys. Rev. Lett. **94**, 052301 (2005).
46. NA49 Collaboration (I. Kraus), J. Phys. G **31**, S147 (2005).
47. A. Mischke *et al.*, Nucl. Phys. A **715**, 453 (2003).
48. NA49 Collaboration (G.I. Veres), Nucl. Phys. A **661**, 383 (1999).
49. NA49 Collaboration (V. Friese), Nucl. Phys. A **698**, 487 (2002).
50. NA49 Collaboration (S.V. Afanasiev *et al.*), Phys. Lett. B **538**, 275 (2002).
51. M. Mitrovski, J. Phys. G **32**, S43 (2006).
52. J. Rafelski, J. Letessier, Acta Phys. Pol. B **34**, 5791 (2003); J. Phys. G **30**, S1 (2004).
53. E917 Collaboration (B.B. Back *et al.*), Phys. Rev. C **69**, 054901 (2004).
54. J. Cleymans, H. Oeschler, K. Redlich, S. Wheaton, Phys. Lett. B **615**, 50 (2005).
55. J. Cleymans, K. Redlich, Phys. Rev. C **60**, 054908 (1999).
56. PHENIX Collaboration (K. Adcox *et al.*), Phys. Rev. C **69**, 024904 (2004).
57. STAR Collaboration (C. Adler *et al.*), Phys. Rev. Lett. **89**, 092301 (2002).
58. PHENIX Collaboration (K. Adcox *et al.*), Phys. Rev. Lett. **89**, 092302 (2002).
59. STAR Collaboration (J. Adams *et al.*), Phys. Rev. Lett. **92**, 182301 (2004).
60. STAR Collaboration (C. Adler *et al.*), Phys. Rev. C **66**, 061901 (2002).
61. C. Adler *et al.*, Phys. Rev. C **65**, 041901 (2002).
62. PHENIX Collaboration (S.S. Adler *et al.*), Phys. Rev. C **69**, 034909 (2004).
63. STAR Collaboration (H.B. Zhang), *Delta, K^* and rho resonance production and their probing of freeze-out dynamics at RHIC*, arXiv:nucl-ex/0403010; STAR Collaboration (J. Adams), Phys. Rev. C **71**, 064902 (2005).
64. STAR Collaboration (C. Markert), J. Phys. G **30**, S1313 (2004).
65. STAR Collaboration (J. Adams *et al.*), Phys. Lett. B **612**, 181 (2005).
66. NA57 Collaboration (D. Elia), J. Phys. G **31**, S135 (2005).
67. BRAHMS Collaboration (I.G. Bearden *et al.*), Phys. Rev. Lett. **94**, 162301 (2005).

68. B.B. Back *et al.*, Phys. Rev. Lett. **91**, 052303 (2003).
69. BRAHMS Collaboration (I.G. Bearden *et al.*), Phys. Rev. Lett. **93**, 102301 (2004).
70. J. Rafelski, Phys. Rep. **88**, 331 (1982).
71. NA57 Collaboration (G.E. Bruno), J. Phys. G **30**, S717 (2004).
72. NA49 Collaboration (C. Alt *et al.*), Phys. Rev. Lett. **92**, 042003 (2004).
73. A.R. Dzierba, D. Krop, M. Swat, S. Teige, A.P. Szczepaniak, Phys. Rev. D **69**, 051901 (2004) [arXiv:hep-ph/0311125].
74. J. Letessier, G. Torrieri, S. Steinke, J. Rafelski, Phys. Rev. C **68**, 061901(R) (2003).
75. Y. Aoki, G. Endrodi, Z. Fodor, S.D. Katz, K.K. Szabo, Nature **443**, 675 (2006) [arXiv:hep-lat/0611014].
76. Y. Aoki, Z. Fodor, S.D. Katz, K.K. Szabo, Phys. Lett. B **643**, 46 (2006) [arXiv:hep-lat/0609068].
77. Z. Fodor, S.D. Katz, JHEP **0404**, 050 (2004) and references therein.
78. C.R. Allton *et al.*, Phys. Rev. D **66**, 074507 (2002).
79. I. Kuznetsova, J. Rafelski, Eur. Phys. J. C **51**, 113 (2007) [arXiv:hep-ph/0607203].
80. J. Rafelski, M. Danos, Phys. Lett. B **97**, 279 (1980).
81. J. Rafelski, J. Letessier, J. Phys. G **28**, 1819 (2002).
82. J. Letessier, A. Tounsi, J. Rafelski, Phys. Lett. B **389**, 586 (1996).
83. J. Rafelski, J. Letessier, Phys. Lett. B **469**, 12 (1999).
84. J. Letessier, J. Rafelski, Phys. Rev. C **75**, 014905 (2007) [arXiv:nucl-th/0602047].
85. P. Braun-Munzinger, K. Redlich, J. Stachel, in *Quark Gluon Plasma 3*, edited by R.C. Hwa, Xin-Nian Wang (World Scientific Publishing, 2004) and references therein.
86. M. Bleicher, J. Aichelin, Phys. Lett. B **530**, 81 (2002).
87. E.L. Bratkovskaya *et al.*, Phys. Rev. C **69**, 054907 (2004).
88. C.R. Allton, M. Doring, S. Ejiri, S.J. Hands, O. Kaczmarek, F. Karsch, E. Laermann, K. Redlich, Phys. Rev. D **71**, 054508 (2005).
89. A. Peikert, F. Karsch, E. Laermann, B. Sturm, Nucl. Phys. Proc. Suppl. **73**, 468 (1999).
90. MILC Collaboration (C. Bernard *et al.*), Phys. Rev. D **71**, 034504 (2005).
91. C.R. Allton, S. Ejiri, S.J. Hands, O. Kaczmarek, F. Karsch, E. Laermann, C. Schmidt, Phys. Rev. D **68**, 014507 (2003).
92. H.Z. Huang, J. Rafelski, AIP Conf. Proc. **756**, 210 (2005).
93. T. Csorgo, J. Zimanyi, Heavy Ion Phys. **17**, 281 (2003).
94. J. Rafelski, J. Letessier, Phys. Rev. Lett. **85**, 4695 (2000).
95. I.I. Roizen, E.L. Feinberg, O.D. Chernavskaya, Phys. Usp. **47**, 427 (2004) [Usp. Fiz. Nauk **47**, 427 (2004)].
96. F. Becattini, M. Gazdzicki, A. Keranen, J. Manninen, R. Stock, Phys. Rev. C **69**, 024905 (2004).
97. E-0895 Collaboration (J.L. Klay *et al.*), Phys. Rev. C **68**, 054905 (2003).
98. B. Pin-zhen, J. Rafelski, Eur. Phys. J. A **32**, 267 (2007).
99. G. Torrieri, J. Rafelski, Phys. Rev. C **75**, 024902 (2007) [arXiv:nucl-th/0608061].